



Tissue metabolism driven arterial tree generation

Matthias Schneider^{a,*}, Johannes Reichold^b, Bruno Weber^c, Gábor Székely^a, Sven Hirsch^a

^a Computer Vision Laboratory, Federal Institute of Technology ETH, Sternwartstrasse 7, 8092 Zurich, Switzerland

^b Institute of Fluid Dynamics, Federal Institute of Technology ETH, Sonneggstrasse 3, 8092 Zurich, Switzerland

^c Institute of Pharmacology and Toxicology, University of Zurich, Rämistrasse 100, 8091 Zurich, Switzerland

ARTICLE INFO

Article history:

Available online 18 May 2012

Keywords:

Arterial tree model
Angiogenesis
Oxygen metabolism
Cerebral vasculature
Computational physiology

ABSTRACT

We present an approach to generate 3-D arterial tree models based on physiological principles while at the same time certain morphological properties are enforced at construction time. The driving force of the construction is a simplified angiogenesis model incorporating case-specific information about the metabolic demand within the considered domain. The vascular tree is constructed iteratively by successively adding new segments in chemotactic response to angiogenic growth factors secreted by ischemic cells. Morphometrically confirmed bifurcation statistics of vascular networks are incorporated to optimize the synthetic vasculature. The proposed method is able to generate artificial, yet physiologically plausible, arterial tree models that match the metabolic demand of the embedding tissue and fulfill the prescribed morphological properties at the same time. The proposed tree generation approach is applied in a simulation setup based on the metabolic configuration and anatomy of the macaque visual cortex. We analyze the generated tree models with respect to morphological and physiological aspects including fluid-dynamic simulations. The comparison of our results with the findings of different studies on the structure of cerebral vasculatures demonstrates the plausibility of our method.

© 2012 Elsevier B.V. All rights reserved.

1. Introduction

1.1. Motivation

Arterial trees are highly complex branching structures for efficient oxygen and nutrient supply of tissue and drainage of metabolic end products (LaBarbera, 1990; Karch et al., 2000). For an in-depth understanding of various aspects of the circulatory system, detailed functional and structural analysis of microvascular networks in both normal and pathological tissue is essential since hemodynamic and metabolic conditions are critically dependent on the microvascular architecture (Secomb et al., 2004; Ji et al., 2006). As an example, detailed, explicit vascular models are needed in surgical training simulation, when generating variable anatomical scenes with realistic physiological properties (Tuchschmid et al., 2007). In the field of cancer research, various models for tumor growth have been proposed which partly rely on explicit vascular models (Lloyd and Székely, 2008). Appropriate validation of these growth models with *in vivo* time-series requires proper initialization with an explicit microvasculature. Similarly, knowledge of the entire cerebrovascular network down to the capillary level is required for gaining insight into blood flow

dynamics and its regulation by numerical simulations (Reichold et al., 2009; Guibert et al., 2010; Lorthois et al., 2011). This allows to assess the significance of occlusions and resulting redistribution of blood flow (Schaffer et al., 2006) as well as the prospective effect of interventions. Additionally, it has been shown that many of the neurodegenerative diseases, e.g., Alzheimer's disease, have a prominent vascular component (Meyer et al., 2008; Zlokovic, 2011). There is increasing evidence that reduced energy substrate and oxygen delivery is in part responsible for the severe symptoms of the disease. This underlines the need for a better knowledge of the vascular network's structure in normal and pathological tissue in order to increase our understanding of the pathophysiological mechanisms.

Microvascular structures have been analyzed based on intravascular dye injections, staining of vessel components, or vascular corrosion casts using state of the art imaging modalities, e.g., all-optical histology (Tsai et al., 2009), or synchrotron radiation based X-ray tomographic microscopy (Plouraboue et al., 2004; Heinzer et al., 2006, 2008; Reichold et al., 2009). However, the segmentation and reconstruction of consistent arterial trees from high-resolution image data still remains a challenge (Cassot et al., 2006; Kaufhold et al., 2008; Risser et al., 2008). While the relatively small number of large vessels can be modeled explicitly, this becomes increasingly difficult for the vast number of smaller vessel branches, e.g., due to the limited spatial resolution of the imaging modality or the lack of image contrast at the microscale. Therefore, numerous methods for the generation of artificial

* Corresponding author. Address: ETF D114.1, Sternwartstrasse 7, CH-8092 Zurich, Switzerland. Tel.: +41 44 63 20379; fax: +41 44 63 21199.

E-mail address: schneider@vision.ee.ethz.ch (M. Schneider).

URL: <http://www.vision.ee.ethz.ch/~schneima> (M. Schneider).

vascular models have been proposed. In this paper we present a physiologically inspired construction approach for arterial models in the absence of pathologies, while relying on case-specific functional information.

1.2. Related work

The main approaches for the generation of artificial vasculatures are typically based on optimality or evolutionary principles. Nekka et al. (1996) describe a deterministic construction method for 2-D vascular structures incorporating a highly simplified angiogenesis model. Vascular formation is modeled as an evolutionary process in response to angiogenic factors secreted by ischemic tissue cells. Vessel segments are considered as 1-D edges in a graph neglecting the spatial extent of the lumen. As the formation process is purely based on the distribution of angiogenic factors without imposing any further restriction regarding the geometry of the evolving network, the results appear rather artificial and too regular. A more sophisticated angiogenesis-based simulation framework for the construction of vascular systems in arbitrary anatomies has been proposed by Szczerba and Székely (2005). This approach has been integrated into a generic model also accounting for tumor growth and modeling (Lloyd et al., 2008). Even though the results show high similarity with real vasculatures, the underlying simplifications still do not allow to generate vascular morphologies in full accordance with experimental findings.

Based on experimental observations from real vessel networks, several optimality principles have long been hypothesized, e.g., minimal building material or minimal energy dissipation (Murray, 1926; Zamir, 1976; Cohn, 1954; Kamiya and Togawa, 1972; Gafiy-chuk and Lubashevsky, 2001; Kassab, 2007). Klarbring et al. (2003) apply strategies originating from topology optimization of electrical networks and load carrying trusses to flow networks. The flow network topology is optimized w.r.t. the cross-section of the pipes in order to minimize the total pressure loss (dissipation) under a total volume constraint.

Schreiner and Buxbaum (1993) proposed to use constrained constructive optimization (CCO) to iteratively construct a 2-D binary tree. The method of CCO (and its variations) is a stochastic construction process purely based on structural optimality principles under hemodynamic boundary conditions. In order to generate visually more realistic vascular trees in 3-D, Karch et al. (1999, 2000) combined CCO with staged tissue growth leading to structural changes of the simulated tree models. However, the vascular trees have been truncated at the prearteriolar scale. Similarly, CCO has recently been combined with time-dependent constraints on a level set distance function to restrict the morphology and the arrangement of major (cerebral) arteries, in particular (Bui et al., 2010). Multiple connected trees, e.g., a venous and arterial tree, can be constructed by connecting new points to both trees inducing two new terminal branches with opposite flow direction specified as boundary condition (Kretowski et al., 2003). This extension of CCO for the construction of multiple coupled trees in 3-D has successfully been applied to simulate biphasic computed tomography images (Kretowski et al., 2007).

Leeuwen et al. (1998) suggested an algorithm for the generation of artificial 3-D vascular networks for use in hyperthermia treatment planning. Formation of new segments starts at uniformly distributed target points in the region of interest towards existing tree segments. The growing process is driven by a 3-D potential field computed as the superposition of potential functions assigned to each established vessel. The driving force is hence defined by the vasculature itself rather than (underperfused) tissue cells. As there is no physiological equivalent to the employed potential field, it remains unclear how to define or adjust the potential to enforce certain physiological properties.

In the aforementioned approaches, tree generation is considered as a strictly generative and irreversible process which does not allow for dynamic remodeling of the vasculature. A more dynamic growth model incorporating vascular degeneration provides the required flexibility to build individual vasculatures meeting prescribed case-specific conditions such as metabolic demand.

1.3. Our approach

We pursue a modeling approach based on a simplified angiogenesis model as the driving force of vascular tree formation and degeneration. It relies on the metabolic activity of the tissue in the considered domain as may be obtained from functional imaging, for instance. At the same time, similar to CCO, we incorporate morphometrically confirmed optimality hypotheses concerning the branching structure of vascular systems. This way, we iteratively build an arterial tree that meets the metabolic requirements of the embedding tissue using a multiscale simulation approach (staged growth). As opposed to previously suggested approaches, we do not explicitly enforce hemodynamic constraints at construction time. Also note, that we focus on the construction of arterial trees rather than a complete vascular network with a venous counterpart.

In Schneider et al. (2011), we sketched a first draft of such an algorithm which was used to construct artificial tree models for different synthetic metabolic maps. In this paper, we significantly extend our previous work, particularly w.r.t. the experimental setup which is based on real data obtained from an animal study on the microvascular structure and oxygen metabolism in the macaque visual cortex (Weber et al., 2008) (see Section 3). The tree construction approach itself is modified to allow for user-defined radius boundary conditions at the initial tree segments (see Section 2.3). In this way, excessive (uncontrolled) growth of single trees is prevented, which ultimately yields more realistic results w.r.t. both morphological and hemodynamic properties. Finally, the synthetic trees are analyzed in more detail w.r.t. morphological, topological, and fluid-dynamic properties.

2. Methods

Our approach for the generation of artificial arterial trees is based on physiological principles related to (sprouting) angiogenesis in order to achieve physiologically plausible results. Angiogenesis describes the formation of new capillary blood vessels from a pre-existing vasculature in well-characterized stages. It plays a crucial role in different growth processes such as embryonic development, wound healing, or tumor growth (Milde et al., 2008). In chemotactic response to angiogenic signals, also known as angiogenic growth factors, solid capillary sprouts develop from pre-existing vessels by means of endothelial cell proliferation and migration towards the source of the angiogenic stimulus. There are numerous growth factors and other chemical substances involved in angiogenesis. We will reduce the complex signaling cascade to a single transmitter, namely the vascular endothelial growth factor (VEGF). This family of transmitters has widely been studied both *in vivo* and *in vitro* and proven to be a potent stimulator of physiological and pathological angiogenesis (Gabhann et al., 2007). VEGF, secreted by, e.g., tumor or ischemic cells, diffuses into the surrounding tissue establishing a concentration gradient between the source and the vessels. In our method, these physiological principles are applied on a gradually growing simulation domain to drive the iterative arterial tree generation consisting of a constructive (growth) and destructive (degeneration) component. In contrast to a purely constructive approach (Schneider et al., 2011), these opposing processes allow for dynamic tree

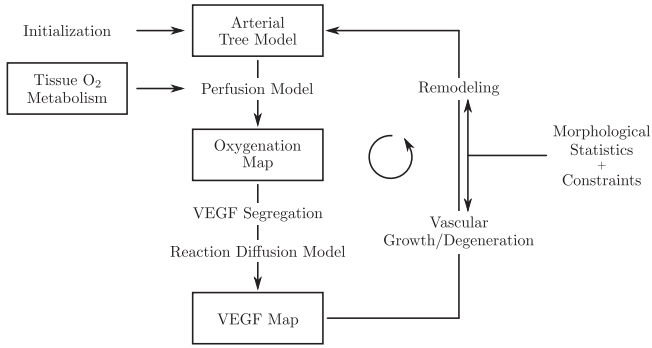


Fig. 1. Schematic workflow of tissue metabolism driven arterial tree generation.

remodeling w.r.t. morphological statistics and constraints as well as the prescribed oxygen metabolism of the embedding tissue. The general workflow of the tissue metabolism driven tree generation is depicted in Fig. 1. The individual components will be explained in further detail in the following.

2.1. Arterial tree model

In this work, we consider arterial tree models rather than full-fledged vascular networks consisting of an arterial supply network and an interconnected venous drainage system. According to morphometric analysis, bifurcations of vascular trees almost invariably branch into two distal branches (Zamir, 1976). As a first approximation, arterial trees can hence be considered as binary trees that can be efficiently represented by a discrete graph structure enhanced by additional node and edge attributes to encode geometry. The graph structure (rooted tree) and the vasculature are related as follows: Each vessel segment is modeled as rigid cylindrical tube with radius r and length l inscribed in the vessel. It is represented by a single directed edge connecting two nodes. Semantically, this gives rise to four different types of nodes, namely root, leaf, bifurcation (\leftarrow), and inter nodes (\rightarrow). The latter links two successive vessel segments and allows to approximate the shape of a tortuous vessel branch. Additionally, each node is tagged with a unique 3-D coordinate $\vec{p} = (x, y, z)^T$. Combining coordinate and connectivity information fully captures the geometry of the approximated vasculature. The edge direction is defined as the direction of blood flow, i.e., pointing “downstream” towards the capillary bed. Note that a binary rooted tree model does not allow for cycles and hence is not able to capture interconnections (anastomoses) and the web-like nature of the capillary network. In the following, we will distinguish between vessel segments and vessel branches. The former denotes a single edge between any two connected nodes, while the latter relates to the path from a bifurcation or root node to the next distal bifurcation or leaf node as a whole. We assume the segment radii of a single branch to be constant, i.e., adjacent edges of an inter node have the same radius (see Fig. 2a).

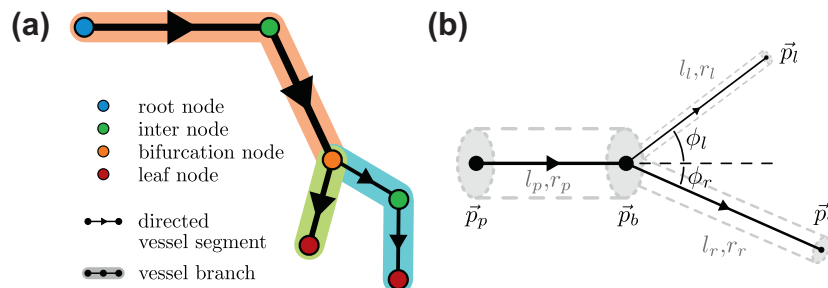


Fig. 2. Arterial tree model (a) with constrained bifurcation configuration (b).

Similar to Schreiner and Buxbaum (1993) and Kretowski et al. (2003), we enforce additional morphological constraints for the arterial tree model. The relation of the decreasing vessel radii from proximal to distal branches is governed by a bifurcation law, also known as Murray's law. It relates the radius of the proximal parent branch r_p to the radius of the left (r_l) and right (r_r) daughter branches (Murray, 1926):

$$r_p^\gamma = r_l^\gamma + r_r^\gamma, \quad (1)$$

where γ denotes the bifurcation exponent, with values reported ranging from $\gamma = 2.0$ to $\gamma = 3.0$ (Arts et al., 1979; Fung, 1997; Schreiner and Buxbaum, 1993; Zamir, 2000). This well-known physiological law has been confirmed by both morphometrical analysis of arterial trees (Zamir, 1976; Kaimovitz et al., 2008) and theoretical considerations on optimality principles (Murray, 1926; Cohn, 1954). However, there are other studies showing that not all bifurcations strictly obey this branching pattern in nature (Cassot et al., 2009). They suggest that while Murray's law is acceptable as a macroscopic approximation, it may not be applicable at all scales, in particular at the microscopic level.

Additionally, the bifurcation configuration is further constrained w.r.t. bifurcation angles based on fluid dynamic considerations (Fung, 1997, Chapter 3.3) and the optimality principles of minimum work and minimum energy dissipation proposed by Murray (1926) and Rosen (1967), respectively:

$$\cos(\phi_l) = \frac{r_p^4 + r_l^4 - r_r^4}{2r_p^2 r_l^2}, \quad \cos(\phi_r) = \frac{r_p^4 + r_r^4 - r_l^4}{2r_p^2 r_r^2}, \quad (2)$$

with ϕ_l , ϕ_r denoting the bifurcation angle of the left and right daughter segment, respectively. Geometrically this corresponds to the optimal position of the branching point \vec{p}_b w.r.t. a minimum volume principle, i.e., minimizing the total lumen volume for fixed boundary points of the adjacent branches:

$$\hat{\vec{p}}_b = \arg \min_{\vec{p}_b} \sum_{k \in \{p, l, r\}} r_k^2 \|\vec{p}_k - \vec{p}_b\|_2, \quad (3)$$

where \vec{p}_p , \vec{p}_l , \vec{p}_r are the boundary nodes of the parent, left, and right segment, respectively (see Fig. 2b).

From a global point of view, arterial vessels share a distinct root, namely the aorta. On a local level, however, the considered vasculature may consist of several disjoint components. Therefore, the arterial tree model has to be extended to a “rooted forest” consisting of several disjoint rooted trees, each of them corresponding to a single arterial component. In the following, we will neglect this subtlety and stick to the term (arterial) tree model.

2.2. Angiogenesis model

We use a simplified angiogenesis model as the driving force for our simulations. The model considers the mutual interplay of arterial oxygen (O_2) supply and VEGF secreted by ischemic cells.

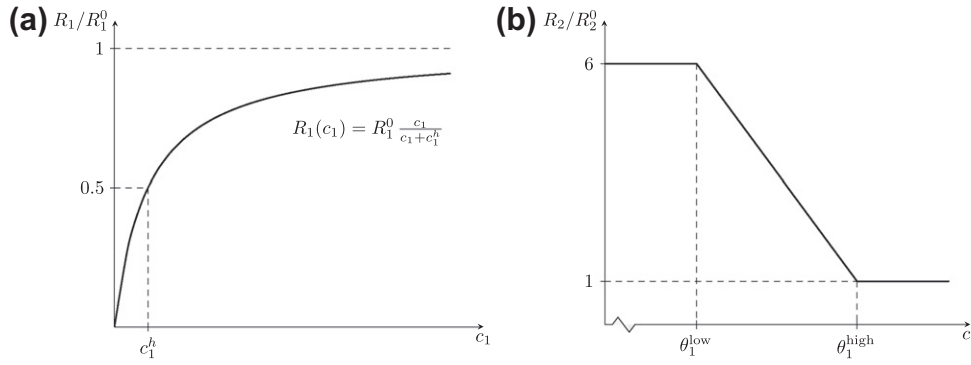


Fig. 3. Michaelis–Menten relationship for the oxygen consumption rate R_1 relative to saturation level R_1^0 as a function of local oxygen concentration c_1 (a). VEGF secretion R_2 relative to base level R_2^0 (b).

Tissue is assumed to be homogeneous w.r.t. O_2 and VEGF transport with diffusivity D_1 and D_2 , respectively. Assuming steady-state conditions, Fick's first law postulates (Secomb et al., 2004):

$$D_1 \nabla^2 c_1 = R_1(c_1), \quad (4)$$

$$R_1(c_1) = R_1^0 \frac{c_1}{c_1 + c_1^h}, \quad (5)$$

where c_1 represents the O_2 concentration. $R_1(c_1)$ denotes the O_2 consumption rate which is modeled by a Michaelis–Menten relationship defined by the O_2 demand at saturation level R_1^0 (unlimited O_2 supply) and the half-saturation concentration c_1^h (see Fig. 3a). Note that R_1^0 is subject to regional variations, in general.

VEGF secretion in tissue is dependent on the average oxygenation level. However, the exact relationship has not yet been experimentally measured. We model the oxygen-dependent VEGF secretion rate R_2 as follows (Gabhann et al., 2007):

$$R_2(c_1) = \begin{cases} 6R_2^0, & \text{if } c_1 \leq \theta_1^{\text{low}} \\ \left(1 + 5 \left(\frac{\theta_1^{\text{high}} - c_1}{\theta_1^{\text{high}} - \theta_1^{\text{low}}}\right)\right) R_2^0, & \text{if } \theta_1^{\text{low}} < c_1 < \theta_1^{\text{high}} \\ R_2^0, & \text{if } c_1 \geq \theta_1^{\text{high}} \end{cases} \quad (6)$$

The shape of R_2 is sketched in Fig. 3b. Along with Eq. (5), the employed thresholds θ_1^{low} and θ_1^{high} have the following interpretation:

$$c_1 = \theta_1^{\text{low}} \Rightarrow \frac{R_1(c_1)}{R_1^0} = \frac{\theta_1^{\text{low}}}{\theta_1^{\text{low}} + c_1^h} \quad (\approx 66.6\%), \quad (7)$$

$$c_1 = \theta_1^{\text{high}} \Rightarrow \frac{R_1(c_1)}{R_1^0} = \frac{\theta_1^{\text{high}}}{\theta_1^{\text{high}} + c_1^h} \quad (\approx 97.6\%). \quad (8)$$

In other words, if the oxygen concentration at a tissue cell exceeds θ_1^{high} , the oxygen saturation level is more than 97.6%. The figures have been computed for the parameter values provided in Table 1.

The secreted VEGF isotropically diffuses and is subject to natural decay while neglecting VEGF uptake by endothelial cells (Milde et al., 2008):

$$D_2 \nabla^2 c_2 = \nu c_2 - R_2(c_1), \quad (9)$$

with VEGF concentration c_2 , diffusivity D_2 , and decay rate ν .

For a given vascular tree, this simplified reaction–diffusion model can be applied in order to approximate the perfusion of the surrounding tissue and to compute the corresponding VEGF concentration map. The transition from the arterial tree model to the O_2 and VEGF map is described in more detail in Appendix A. In brief, the oxygenation map is approximated as the superposition of the oxygenation induced by each single vessel segment according to Eq. (4). We assume radial O_2 diffusion with a Dirichlet boundary condition on the surface of the artery wall. The boundary

Table 1

Main simulation parameters. The default values are underlined (if required). Additional algorithm parameters are listed in Table B.3.

Parameter	Value	Unit	Source	Text
D_1	2.41×10^{-9}	$\text{m}^2 \text{s}^{-1}$	Ji et al. (2006)	Eq. (4)
$R_{O_2}^{\text{base}}$	5.08×10^{-4}	$\text{m O}_2 \text{m}^{-3} \text{s}^{-1}$	Powers et al. (1985)	Eq. (5)
c_1^h	1.95×10^{-5}	$\text{m O}_2 \text{m}^{-3}$	Ji et al. (2006)	
κ	4.08×10^{-3}	$\text{m O}_2 \text{m}^{-3} \text{m}_{\text{blood}}^{-3}$	n/a	Eq. (A.1)
r_0	3.5×10^{-6}	m	Cassot et al. (2006)	
θ_1^{low}	3.89×10^{-5}	$\text{m O}_2 \text{m}^{-3}$	Gabhann et al. (2007)	Eq. (6)
θ_1^{high}	7.78×10^{-4}	$\text{m O}_2 \text{m}^{-3}$	Gabhann et al. (2007)	
D_2	1.04×10^{-10}	$\text{m}^2 \text{s}^{-1}$	Gabhann et al. (2007)	Eq. (9)
ν	$4 \times 1.81 \times 10^{-4}$	s^{-1}	Milde et al. (2008)	
γ	<u>3.0</u> , 3.5	–	Fung (1997)	Eq. (1)
m_b	12, <u>14</u> , 16	–	n/a	Eq. (10)
v_b	6.0	–	n/a	
λ_g	1.0	–	n/a	Eq. (12)
ψ	1.1	–	n/a	Eq. (15)
r_{min}	3.0×10^{-6}	m	n/a	

condition is chosen heuristically based on a radius-dependent scheme that makes small vessels at the capillary scale contribute most to the oxygenation, whereas large vessels have a negligible effect (see Appendix A for details). The induced steady-state VEGF concentration is subsequently computed according to Eqs. (6) and (9). Corresponding to the physiological principle of sprouting angiogenesis, the VEGF concentration map is then used as an excitatory potential field for vascular growth.

2.3. Vascular growth

Following the process of sprouting angiogenesis, vascular growth is modeled as a chemotactic process w.r.t. the local VEGF concentration. In other words, we will consider vascular growth as a predominantly local process, i.e., the vasculature is being adapted and remodeled locally in order to counteract the secretion of a growth-stimulating external VEGF agent. The vascular growth model is sketched in Algorithm 4 in Appendix B. In general, we distinguish between apical growth at leaf nodes (apices) and sprouting at inter nodes.

2.3.1. Apical growth

Apical growth is the primary growth process observed in nature. A capillary may either elongate or bifurcate into two similar branches resulting in mostly symmetric bifurcations. We model

this binary event as a probabilistic process, which directly allows to incorporate further constraints on the morphology (branching pattern) of the constructed tree structures. To this end, we prescribe a global branch length statistics assuming the branch aspect ratios $x = l/r$ follow a log-normal distribution with location and scale parameter μ_b and σ_b , respectively:

$$p_b(x) = \log \mathcal{N}(x; \mu_b, \sigma_b) = \frac{1}{x\sqrt{2\pi\sigma_b^2}} \exp\left(-\frac{(\ln x - \mu_b)^2}{2\sigma_b^2}\right), \quad (10)$$

where $x = l/r$ denotes the aspect ratio of a branch with (constant) radius r and (cumulative) length l . Using the corresponding cumulative distribution function (cdf) of this branch length distribution, an evolving leaf node at the distal end of a vessel branch with aspect ratio $x = l/r$ will form a bifurcation with probability:

$$P_b(x; \mu_b, \sigma_b) = \Phi\left(\frac{\ln x - \mu_b}{\sigma_b}\right) = \frac{1}{2} + \frac{1}{2} \operatorname{erf}\left(\frac{\ln x - \mu_b}{\sqrt{2}\sigma_b}\right), \quad (11)$$

where $\Phi(x)$ denotes the standard normal cdf and $\operatorname{erf}(x)$ the Gaussian error function.

In case of an elongation at a leaf node \vec{p} , the growth direction is chosen based on the local VEGF gradient as

$$\vec{d}_g = \frac{\nabla c_2(\vec{p})}{\|\nabla c_2(\vec{p})\|} + \lambda_g \frac{\vec{d}_s}{\|\vec{d}_s\|}, \quad (12)$$

where $\|\cdot\|$ denotes the Euclidean norm, \vec{d}_s the (oriented) direction of the proximal segment and λ_g a constant regularizer to avoid sharp bendings. The radius of the new distal segment is adopted from the proximal segment. For given segment radius, the corresponding segment length is inferred from the branch length statistics in Eq. (10) to completely define the newly formed segment.

In case of a bifurcation at a leaf node, the segment radii r_1, r_2 of the two new distal branches are computed based on the proximal segment radius r_p :

$$\begin{aligned} r_c &= 2^{-1/\gamma} r_p, \\ r_1 &\sim \mathcal{N}(r; \mu = r_c, \sigma = r_c/32), \\ r_2 &= (r_p^\gamma - r_1^\gamma)^{1/\gamma}. \end{aligned} \quad (13)$$

Intuitively, this heuristic has the following interpretation: For given proximal segment radius r_p , we compute the “expected” radius r_c of the distal segments according to Murray’s law for a fully symmetric bifurcation ($r_1 = r_2$). Next, r_c is used as the mean of a narrow normal distribution to infer r_1 . Finally, r_2 is well-defined according to Murray’s law given r_p and r_1 . Strictly speaking, we further restrict the valid radius range to $r_{\min} \leq r_1, r_2 \leq r_p$ in order to avoid both excessively strong growth and tiny sprouts ($r_{\min} = 3 \mu\text{m}$). Just like the elongation case, the segment lengths are inferred from the branch length statistics for given segment radii. The branching angles are computed using Eq. (2).

According to the minimum volume principle, the adjacent segments at a bifurcation node are coplanar (Kamiya and Togawa, 1972; Fung, 1997). We define the corresponding plane at a bifurcating leaf node to be spanned by the direction of the proximal segment and the local VEGF gradient. In this way, the bifurcation configuration is well-defined except for the arbitrary ordering of the left and right segment. Applying the branching angles directly, however, might result in large deviations of the grow directions from the local VEGF gradient. Therefore, we finally adjust this tentative bifurcation configuration as follows: Firstly, the distal segments are ordered (left vs. right) such that the enclosed angle of the larger segment and the the VEGF gradient becomes minimal. Next, both segments are rotated about the normal vector of the

bifurcation plane such that the larger segment coincides with the VEGF gradient. Finally, the bifurcation node is relocated using Eq. (3) in order to reinforce optimal bifurcation angles.

2.3.2. Sprouting

Besides apical growth at leaf nodes, vessels may also build sprouts at inter nodes resulting in both symmetric and asymmetric bifurcations. Forming a new sprout at an inter node divides the pre-existing vessel into a proximal and distal branch with aspect ratio x_p and x_d , respectively. Consequently, introducing the new sprout affects the tree’s branch length statistics as a single branch is replaced by two shorter ones (and the new sprout is added). Hence, we define the sprouting probability at an inter node using Eq. (11) as:

$$P_s(x_p, x_d; \mu_b, \sigma_b) = \sqrt{P_b(x_p; \mu_b, \sigma_b) P_b(x_d; \mu_b, \sigma_b)}. \quad (14)$$

Intuitively, this definition makes sprouting less likely towards the source and target of a vessel branch and more likely towards the center.

Similar to apical growth, we choose the local VEGF gradient as the preferred growth direction of the new sprout: $\vec{d}_g = \frac{\nabla c_2(\vec{p})}{\|\nabla c_2(\vec{p})\|}$. In order to prevent the new sprout from growing in the direction of the (pre-existing) distal branch, we apply an additional angular condition. For this, we allow for sprouting only if the local VEGF gradient \vec{d}_g and the direction of the distal branch draw an angle of at least 10° . The new segment radius r_s is computed as

$$\begin{aligned} r'_p &= \psi \cdot r_p, \\ r'_s &= (r_p^{\gamma'} - r_p^\gamma)^{1/\gamma} \\ &= (\psi^\gamma - 1)^{1/\gamma} r_p, \\ r_s &= \begin{cases} r \sim \mathcal{U}(r_{\min}, r'_s), & \text{if } r_{\min} < r'_s \\ r_{\min}, & \text{otherwise} \end{cases} \end{aligned} \quad (15)$$

where r_p denotes the radius of the (prospective) parent segment and $\psi > 1$ a “growth stimulator” (see below). This definition has the following motivation. According to Murray’s law, generating the new sprout at the inter node results in either enlargement of the proximal segment or narrowing of the distal segment (or both). Crude downsizing of the distal segment may have severe implications on the morphological and functional properties of the distal subtree. Therefore, we in fact try to maintain the radius of the distal segment and compensate for the additional blood demand by enlarging the proximal segment accordingly. To this end, we define the scaling factor $\psi > 1$ that determines the maximum dilation r'_p of the proximal segment. Given this upper bound, we keep the distal segment’s radius unchanged at r_p and compute the resulting “expected” radius r'_s for the new sprout according to Murray’s law. Finally, we randomly choose the new segment radius r_s from the interval $[r_{\min}, r'_s]$ using a uniform distribution (\mathcal{U}). The choice of ψ effectively determines the upper bound of r_s , e.g., $r'_s = 0.331 r_p$ for $\psi = 1.1$ and $\gamma = 3$.

For given segment radius r_s , the segment length is inferred from Eq. (10) and the proximal segment radius is adjusted using Murray’s law. Growth direction, segment radius and length uniquely define the new sprout. However, the resulting bifurcation configuration is non-optimal w.r.t. bifurcation angles. Similar to the bifurcation case, we optimize the tentative bifurcation configuration by relocating the bifurcation node according to Eq. (3).

2.4. Tree remodeling

As sprouting inter nodes and bifurcating leaf nodes in general spoil the bifurcation law on a global scale, additional tree remodel-

ing is required to reinforce global optimality of the evolving vascular tree model. Local adaption of a single vessel branch hence implicates global effects on the morphology of the entire vascular tree.

In a first step, the segment radii are being updated along the path from the site of growth up to the root node according to Murray's law. Adjusting the radii, in turn, impairs the optimality of branching angles. Therefore, bifurcation optimality is recovered by relocating non-optimal bifurcation nodes according to Eq. (3). Applying this back-propagation scheme for vessel radii results in continuously growing tree segments as investigated in our previous work (Schneider et al., 2011). Depending on the initial conditions, this may produce rather unrealistic morphologies due to the inherent assumption of unlimited blood and oxygen supply at the root nodes. Prescribing the vessel radius at each root segment easily circumvents this phenomenon but requires further adjustment in order to reinforce the additional boundary condition. If the radius of the root segment r deviates from the prescribed radius r_0 after back-propagation ($r' \neq r_0$), all tree segments have to be rescaled by r_0/r' . This symmetric rescaling with constant scaling factor does not affect the validity of Murray's law nor the optimality of the bifurcation angles (see Eqs. (1) and (2)). The rescaling might reduce the radius of some tree branches to unreasonably small values. Therefore, we iteratively prune tiny terminal segments with radius $r < r_{\text{prune}}$, where r_{prune} denotes a constant radius threshold. The pruning step will be explained in more detail in the next section. The different steps for tree remodeling are summarized in Algorithm 5 in Appendix B.

2.5. Vascular degeneration

Vascular growth is a highly dynamic process subject to continuous reorganization. This comprises not only the formation of new sprouts but also the reorganization and degeneration of non-utilized vascular structures (Kurz et al., 2003). For our tree construction, we rely on a simplified vascular degeneration step which counterbalances the generative growth process and thus allows for morphological reorganization to a certain extent. The degeneration proceeds in three steps:

First of all, we shrink prominent terminal branches. It is well known that in the (normal) circulatory system, the arterial and venous part are connected by the capillary bed. Aside from prearterioles and arteriovenous shunts (Pries et al., 2010), which are neglected in our tree model anyway, blood cells pass the capillary network to deliver oxygen and nutrients on their path from the arterial to the venous side. Therefore, the terminal branch radii of our tree model should ultimately be in the capillary range. Non-capillary terminal segments can occur due to the choice of the segment radius in the constructive growth process but also due to vascular degeneration itself (see below). We try to overcome this problem by shrinking terminal branches with radius $r > r_{\text{degen}}$. The reduced radius is computed by linear interpolation as $r' = (1 - \lambda_s)r + \lambda_s r_{\text{prune}}$. In order to recover the consistency, the vascular tree has to be remodeled subsequently as explained in Section 2.4.

In the second step, potentially unnecessary vessel segments are being pruned. Intuitively, one could think of fluid dynamic measures, e.g., blood flow rate at terminal segments, to decide whether or not a capillary should be sustained or not. This would require a full-fledged multiphysics simulation of the fluid dynamic properties of the tree model after each iteration, which is computationally expensive, though. What is more, setting reasonable boundary conditions at the root and terminal segments is difficult since the evolving tree model does not represent a meaningful vasculature until the end of the construction process. We therefore use a more heuristic approach to judge the importance of a capillary sprout in

the first place, namely the VEGF concentration. If the local VEGF concentration at any terminal node falls below a certain threshold, we consider the corresponding terminal segment as potentially dispensable. Since this is a somewhat vague criterion, we discard each candidate segment only with a small probability in order to avoid excessive pruning.

Finally, we supplement the VEGF criterion by the employed branch length statistics in Eq. (10). If the bifurcation probability at a terminal node exceeds a threshold close to 1, this is a good indicator that the terminal branch shows an abnormally high aspect ratio, i.e., the branch is abnormally long for given vessel radius. In this case we prune the corresponding leaf segment in order to counteract this deviation.

Tree remodeling is required once more when pruning an entire vessel branch which may consist of a single vessel segment only. Removing the terminal branch converts the proximal source node of the branch from a bifurcation node to an inter node. In order to recover consistency of the inter node configuration, we rescale the distal subtree radii by r_p/r_d , where r_p and r_d denote the segment radii of the proximal and distal segment, respectively. Additionally, we relocate the former bifurcation node in order to smoothen the resulting branch. The new location is chosen as the center of the neighboring proximal and distal node.

Pseudo code for the vascular degeneration and the pruning of terminal vessels is provided in Algorithms 6 and 7 in Appendix B.

2.6. Iterative tree construction

Finally, we are able to put together the different building blocks that have been presented in the previous sections to a self-contained tree construction algorithm. It pursues an iterative multiscale approach as summarized in Algorithm 2 in Appendix B. We will first explain the iterative construction and address the multiscale aspect at the end of this section.

The input to the algorithm is an initial tree model, a metabolic map indicating the oxygen metabolism of the surrounding tissue and a simulation domain. The initial tree is then iteratively refined as follows: In a first step, the total oxygenation along with the induced steady-state VEGF concentration map are computed on the simulation domain as explained in Section 2.2 and Appendix A in more detail. Following the basic principle of sprouting angiogenesis, the VEGF field is then used to find excited tree nodes that are potential candidates for vascular growth in response to the VEGF stimulus. To this end, we uniformly sample a set of random N_p points from the simulation domain and pick the one with maximum VEGF concentration. From the randomly sampled points, the picked one hence indicates the "hot spot", i.e., the location of highest VEGF signaling as a result of hypoxic tissue cells lacking oxygen supply. From the N_n closest tree nodes to this hot spot, we again choose the node \bar{p} with maximum VEGF concentration as the presumably best suited node to counteract the local VEGF stimulus. If the VEGF concentration at node \bar{p} exceeds a critical threshold θ_c , we consider this node to be excited and hence locally refine the tree model using the mechanisms for vascular growth and tree remodeling as explained in Sections 2.3 and 2.4. The remodeled tree is then used as input for the next iteration. This process is repeated until the tissue cells in the simulation domain are sufficiently perfused. A single cell is considered sufficiently perfused if the local oxygen consumption exceeds θ_1^{high} , i.e., the cell does not secrete any extra VEGF in the sense of Eq. (6). Based on this, the entire domain is defined as sufficiently perfused if the ratio of perfused cells (voxels) to the total number of cells (voxels) exceeds the threshold θ_p .

The iterative tree construction is encapsulated in a multiscale framework. The simulation scale has been introduced to emulate virtual staged growth of the simulation domain (tissue) starting from a downscaled instance to the real simulation domain. In fact,

the simulation scale $s > 0$ defines a coordinate transformation T_s mapping from the real domain Ω_0 (world coordinates) to the re-scaled simulation domain Ω_s (simulation coordinates):

$$T_s : \Omega_0 \rightarrow \Omega_s \quad (16)$$

$$\vec{x} \mapsto s_0 \frac{N_s - s}{N_s - 1} \cdot \vec{x},$$

where s_0 denotes the initial scale and N_s the total number of scales. In particular, T_{N_s} is the identity. The arterial tree models can be transformed similarly by scaling all tree node coordinates and linear measures, e.g., vessel radii.

Finishing the generative growth phase for a given simulation scale, we perform a tree degeneration step as described in Section 2.5 before advancing to the next scale. During the iterative growth phase, a somewhat alleviated degeneration strategy is applied which only affects leaf nodes with low VEGF concentration. If a leaf node is being sampled as the best suited candidate close to the hot spot but not excited due to low local VEGF concentration, the corresponding leaf segment is being pruned.

3. Numerical experiments and analysis

3.1. Experimental setup

The proposed iterative tree construction approach was applied in an experimental setup that is geared to the cerebral anatomy and physiology. The simulation domain is defined as an axis-aligned cuboid with its longitudinal axis orthogonal to the cortex surface ($z = 0$). For subsequent analysis, we further define a cylindrical region of interest (ROI) that is located in the center of the simulation domain as shown in Fig. 4a.

The steady-state metabolic demand of the tissue is approximated by measurements of cytochrome oxidase (COX) activity following Weber et al. (2008). In this study, COX staining has been applied to the macaque visual cortex V1 in order to measure the COX activity along the cortical depth (Weber et al., 2008, Fig. 4). We apply a linear transformation to map the relative COX measurements to the absolute cerebral metabolic rate of oxygen consumption, where the base consumption rate is set to $R_{O_2}^{\text{base}} = 5.08 \times 10^{-4} \text{ mO}_2 \cdot \text{m}_{\text{tissue}}^{-3} \cdot \text{s}^{-1}$ assuming an average brain density of 1.05 g/ml (Powers et al., 1985). Cubic spline interpolation is used to compute a continuous metabolic profile which is embedded in the simulation domain as shown in Fig. 4b.

The tree construction is initialized by descending cortical vessel stubs perpendicularly plunging into the cortex. To this end, microscopic images of the pial network of the macaque visual cortex have been used to segment the entry points on the cortex surface as shown in Fig. 4c. According to the entry point map and the COX profile, the dimensions of the box-shaped simulation domain Ω are chosen as $992 \times 864 \times 1760 \mu\text{m}^3$. For the cylindrical ROI \mathcal{R} we set

the height to $1536 \mu\text{m}$ and the major and minor diameters to $648 \mu\text{m}$ and $552 \mu\text{m}$, respectively. The domains are discretized by a regular grid with an isotropic voxel spacing of $32 \mu\text{m}$. As illustrated in Fig. 4a, the length of the initial stubs is set to $l = 100 \mu\text{m}$ with a normally distributed radius $r = 15 \pm 1.25 \mu\text{m}$ (Weber et al., 2008).

All simulations are conducted for $N_s = 16$ scales. The initial scaling factor s_0 is chosen such that the radius of the smallest initial vessel stub is mapped to the absolute minimum radius $r_{\text{prune}} = 2 \mu\text{m}$ at the initial scale $s = 1$ (see Eq. (16)). In order to account for statistical variation of the constructed trees, all simulations are repeated four times using different seeds for the employed pseudo random number generator (PRNG). The default simulation parameters are summarized in Table 1. Note that we use the mean m_b and variance v_b to parametrize the log-normal branch length distribution of Eq. (10).

Fig. 5 visualizes the evolving vasculature at different scales for a single realization using the default parameter set. Single connected tree chunks are displayed separately for different simulation parameters in Fig. 6.

We have analyzed the constructed arterial tree models with regard to their structural and functional properties. For now, we consider the simulations for the default parameter set.

3.2. Global morphometry

For the morphometrical analysis we consider vessel segments within the ROI only. In this way, the influence of artifacts close to the boundary of the simulation domain are being reduced. First of all, we analyzed the characteristics of the length and diameter distributions over all vessel branches (within the ROI). In accordance with Lauwers et al., 2008, the logarithm of the length and the inverse of the square root of the segment diameter can be approximated by a normal distribution with similar mean and median, skewness close to zero, kurtosis close to three (see Fig. 7). The sharp peak at $d = 6 \mu\text{m}$ in the normalized diameter distribution results from the choice of the minimum radius $r_{\text{min}} = 3 \mu\text{m}$.

Besides branch diameter and length, we also investigated the bifurcation configurations w.r.t. the optimality principles of our arterial tree model, namely Murray's law and the optimality of bifurcation angles (see Eqs. (1) and (2)). The former is strictly enforced intrinsically by design of the algorithm. The latter, in contrast, is applied as a soft constraint, i.e., we allow for small deviations ($\theta_a = 5^\circ$) from the supposedly optimal bifurcation angle. Computing the average angular deviations for all bifurcation nodes, we note that the differences stay well below the tolerance θ_a as shown in Fig. 8a.

In order to compare our tree model to the prescribed branch length statistics, we compute the aspect ratio $x = l/r$ for each

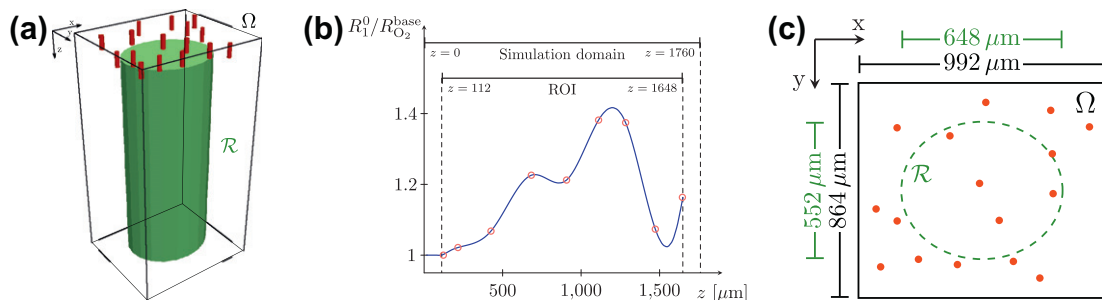


Fig. 4. (a) Box-shaped simulation domain Ω with inscribed cylindrical region of interest \mathcal{R} . The initial stubs on the cortex surface ($z = 0$) are rendered as red cylinders with normally distributed radius $r = 15 \pm 1.25 \mu\text{m}$ and constant length $l = 100 \mu\text{m}$, respectively. (b) Metabolic activity R_1^0 relative to base consumption rate $R_{O_2}^{\text{base}}$ as a function over cortical depth z based on COX data (red circles) taken from Weber et al. (2008, Fig. 4). The black bars indicate the depth range of the simulation domain and the ROI. (c) Arterial entry point map on the cortex surface for simulation domain Ω . The dashed ellipse outlines the region of interest \mathcal{R} .

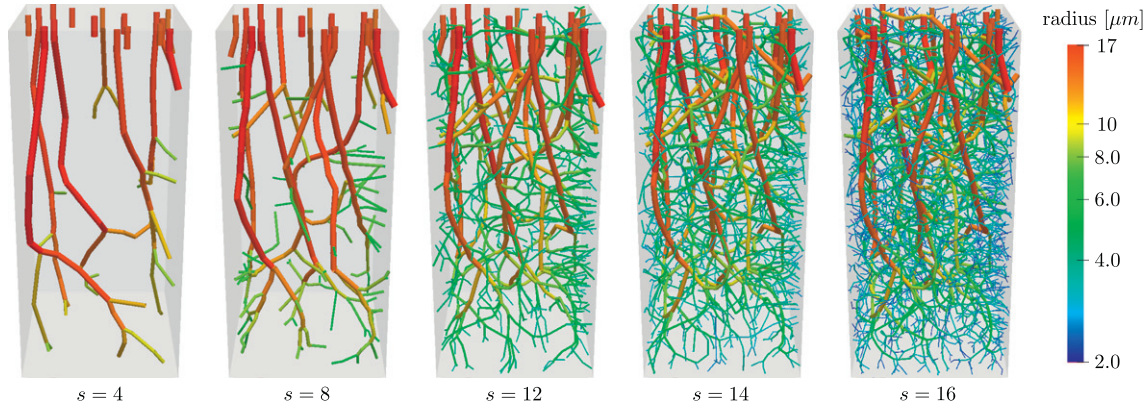


Fig. 5. Evolution of an arterial tree model at different scales s . The simulation domains have been rescaled to the size of the target domain (right) for better comparability. The segment radii are color-coded on a logarithmic scale. (For interpretation of the references to color in this figure legend, the reader is referred to the web version of this article.)

branch within the ROI, where l and r are the branch length and diameter, respectively. The aspect ratio distributions are plotted along with the prescribed log-normal distribution of Eq. (10) for different mean values in Fig. 8b–d.

3.3. Topology

For the topological analysis, we classify vessel branches according to the well-established diameter-defined Strahler system introduced by Kassab et al. (1993). In this classification scheme, leaf segments are assigned Strahler order zero. The Strahler order of the remaining branches is iteratively computed along the path from the leaf segments towards the root node. Based on the Strahler order, consecutively connected vessel branches of the same order form a Strahler vessel.

The diameter-defined Strahler orders of a single connected component is illustrated in Fig. 9a. Note that the topological analysis based on the Strahler system is only meaningful on the uncropped trees, i.e., also including vessel segments outside the ROI. The semi-log plot of Fig. 9b shows the total number of Strahler vessels per Strahler order. Similarly, the semi-log plot of Fig. 9c relates the Strahler order to the average length and diameter of the Strahler vessels.

3.4. Microvascular structure

We further analyzed the microvascular structure of the tree models. Common characteristics for microvascular analysis are the volume fraction and length density which have proven to strongly correlate with the steady-state metabolic demand of the tissue (Weber et al., 2008). In order to validate these findings for our models, we have repeated our simulations with the same input parameters but constant metabolic activity throughout the entire simulation domain. The metabolic level was set to the base level, i.e., each cell metabolizes oxygen at the constant rate $R_{O_2}^{\text{base}}$. The resulting microvascular structures have been analyzed and compared to the original trees for the COX-based metabolism. To this end, the simulation domain was sliced along the z -axis into thin slabs of height $64 \mu\text{m}$. The average length density and volume fraction of the microvascular structure was then computed for each slab. Vessels with a diameter of less than $8 \mu\text{m}$ were considered to be capillaries (Weber et al., 2008). The analysis was again restricted to the ROI in order to exclude boundary artifacts. Fig. 10 compares these quantitative descriptors of the microvasculature across the cortical depth for the two different models.

3.5. Hemodynamic analysis

A simulation framework proposed by Reichold et al. (2009) was used to simulate the pressure and blood flow through the tree model which is treated as a flow network in this context. The resistance of each (vessel) segment is computed based on the Hagen-Poiseuille equation where the viscosity follows the *in vivo* effective blood viscosity taking into account the local hematocrit as well as the endothelial surface layer (Pries and Secomb, 2005). Pressure boundary conditions are set at the feeding arteries (root nodes) and the capillaries (terminal nodes) using literature values (Lipowsky, 2005). The pressure and flow information was used to perform a basic plausibility check w.r.t. the balance of oxygen supply and demand. The total oxygen consumption rate within the ROI \mathcal{R} is $Q^- = \iiint_{\mathcal{R}} R_i^0(z) dx dy dz$, where $R_i^0(z)$ is the metabolic activity at cortical depth z (see Fig. A.12b). For the parameters of our experimental setup, this yields $Q_{\text{const}}^- = 219 \text{ pl/s}$ assuming constant metabolic level $R_i^0 = R_{O_2}^{\text{base}}$ and $Q_{\text{cox}}^- = 264 \text{ pl/s}$ for the COX profile of Fig. 4b. The total amount of oxygen delivered by the vasculature can be approximated based on the following considerations. The concentration of oxygen in blood can be computed as

$$c_{O_2} = 1.34 \text{ ml/g } c_{\text{Hb}} s_{O_2} + 0.003 \text{ ml/dl mmHg } p_{O_2}, \quad (17)$$

where c_{Hb} denotes the hemoglobin concentration in blood, s_{O_2} the oxygen saturation of hemoglobin, and p_{O_2} the partial pressure of oxygen in blood. Assuming $c_{\text{Hb}} = 15 \text{ g/dl}$ and $p_{O_2} = 95 \text{ mmHg}$, this yields $c_{O_2}^{\text{in}} = 191.8 \mu\text{l/ml}$ at the feeding vessels ($s_{O_2} = 94\%$), respectively $c_{O_2}^{\text{out}} = 153.6 \mu\text{l/ml}$ at the capillaries for $s_{O_2} = 0.75$ (Boas et al., 2008). Using these values, the total amount of oxygen delivered by the vasculature to the cells within the ROI can be approximated as $Q^+ = (c_{O_2}^{\text{in}} - c_{O_2}^{\text{out}}) \sum_t Q(t)$, where $Q(t)$ denotes the blood flow rate at terminal segment t .

We have performed a small parameter study to investigate the influence of different simulation parameters on the flow-dynamic properties of the tree models. For this, the simulations have been repeated for the COX-based and the constant metabolic level with the mean value of the branch length statistics $m_b \in \{12, 14, 16\}$ and Murray's exponent to $\gamma \in \{3.0, 3.5\}$. The remaining parameters are left unchanged. Each simulation is repeated four times with different seeds for the PRNG. The resulting pressure and flow velocity distributions for the different parameter sets are illustrated in Fig. 11 along with the reference values from Lipowsky (2005). The corresponding values of oxygen supply (Q^+) and demand (Q^-) are listed in Table 2.

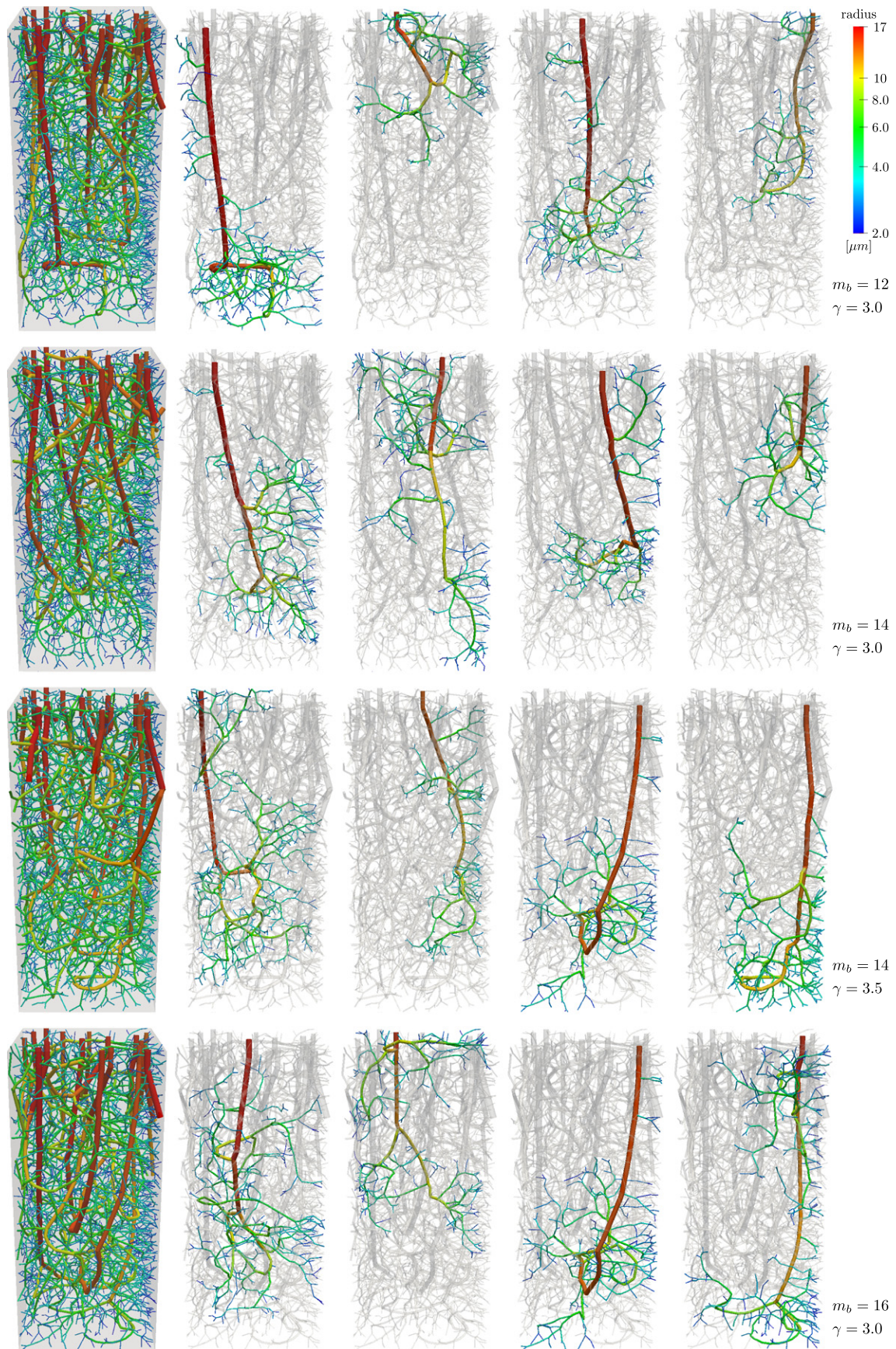


Fig. 6. Synthetic tree models for different simulation parameters. Left: Complete tree model. Right: Isolated single connected tree components. The segment radii are color-coded on a logarithmic scale. (For interpretation of the references to color in this figure legend, the reader is referred to the web version of this article.)

	Mean \pm Sigma	Median	Skewness	Kurtosis
Diameter d [μm]	8.22 ± 4.49	6.73	2.47	10.56
$1/\sqrt{d}$	0.37 ± 0.07	0.39	-0.57	2.72
Length l [μm]	60.18 ± 46.56	45.80	1.89	7.71
$\log l$	3.84 ± 0.74	3.82	-0.14	2.97

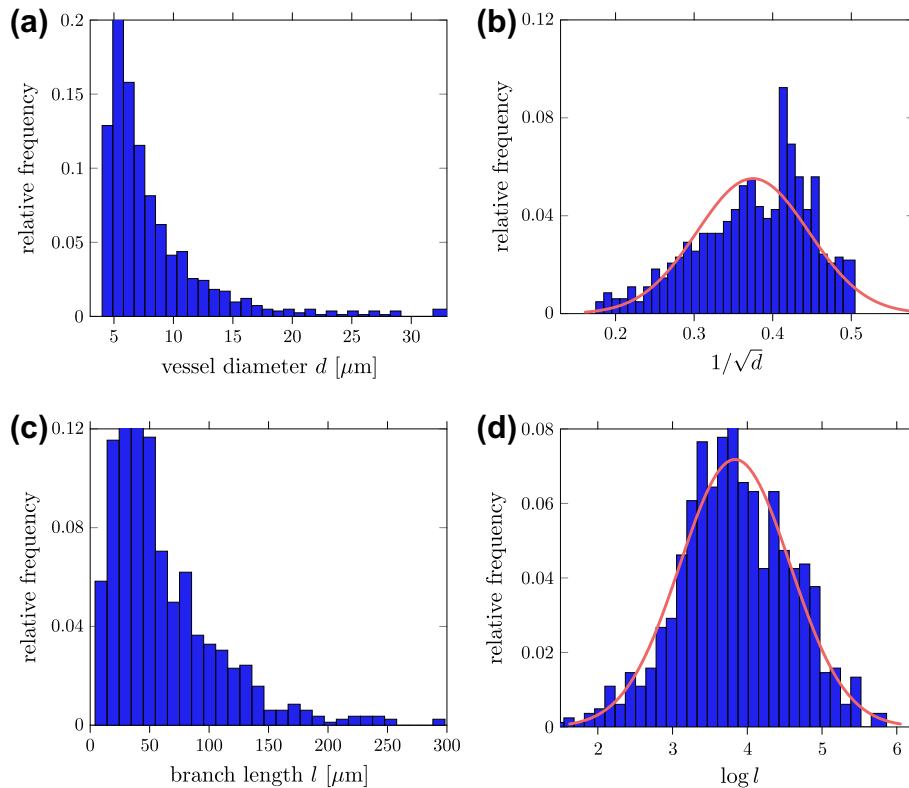


Fig. 7. Characteristics of segment length l and diameter d distributions computed over all vessel segments within the ROI. In accordance with Lauwers et al., 2008, the distribution of the diameter (a) and the branch lengths (c) can be normalized by the inverse of the square root (b) and the logarithm (d), respectively.

4. Discussion

The presented angiogenesis and vascular growth models involve many parameters. Even though some of them have a direct interpretation and can partly be chosen based on literature values, it is still difficult to predict their ultimate influence on the outcome. We have performed small sensitivity studies to investigate the effect of the different parameters on the structural and functional properties of the tree by individually varying a single parameter in a reasonable range while fixing the others at the reported default values. In the presented experimental results, we show the effect of two factors we found most significant, namely the metabolic demand of the surrounding tissue and the branching pattern including Murray's exponent and the prescribed branch length statistics. A more extensive sensitivity analysis of the parameters without reference values from the literature using brute-force grid search is computationally prohibitive considering the algorithmic complexity. Besides, the lack of effective quality criteria renders a rigorous and compact evaluation of different parameter configurations very difficult.

As described in Section 2.4, tree remodeling has global effects on the morphology of the vascular model. Therefore, the perfusion and VEGF concentration maps have to be recomputed after each iteration, which clearly represents the computationally most expensive operation involved in the generation process. In spite of the numerical optimization of the angiogenesis model (see Appendix A), the total computation time for the simulations pre-

sented in Section 3 is still about three hours in average, while certainly depending on the parameter values using a multi-threaded C++ implementation on state-of-the-art hardware (quad-core CPU at 2.8 GHz and 8 GB of RAM).

Explicit comparison of the synthetic tree models with real vascular systems is difficult. Considering the structural complexity and the inherently stochastic nature of vessel formation, particularly at the microvascular scale, comparing functional properties and structural statistics is a reasonable approach to investigate the similarity of vascular structures.

From a visual point of view, the synthetic trees correspond well to real cerebral arteries reported in the literature (Cassot et al., 2006; Weber et al., 2008; Cassot et al., 2010), even if the microvascular structures are not modeled with the required complexity as a result of the binary tree model. Vasculatures close to the boundary of the simulation domain are notably affected by simulation artifacts and show abnormal structures. For this reason, the analysis of the generated vasculature has been restricted to the ROI whenever possible.

Morphological analysis reveals good agreement of the branch length distribution with the prescribed statistics. This result cannot be taken for granted. Even though each single branch is created according to the reference statistics, all branches undergo heavy remodeling in the course of the iterative construction process. Nonetheless, the overall distribution is largely preserved with slight deviations especially for small aspect ratios (see Fig. 8b–d). We also note a small peak on the right shoulder of the distribution

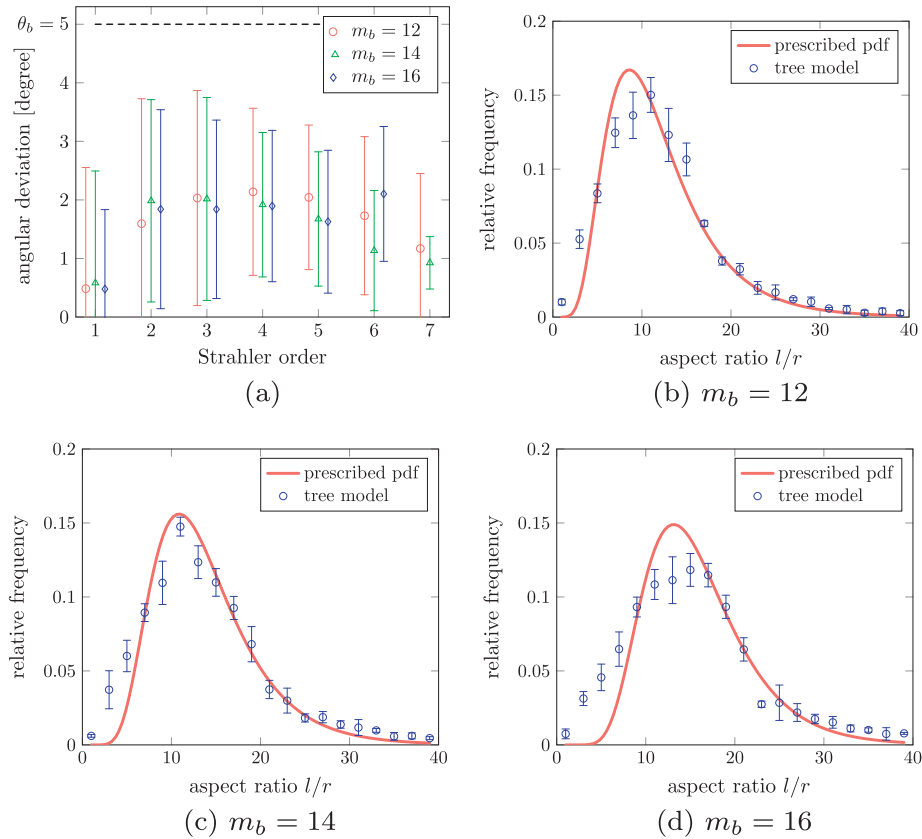


Fig. 8. (a) Average bifurcation angle deviation over diameter-defined Strahler order for different simulation parameters. The correction threshold $\theta_a = 5^\circ$ is indicated by the dashed line. (b)–(d) Comparison of prescribed branch length statistics with the average frequency of the aspect ratio l/r over all vessel branches within the ROI for different statistics parameters. The error bars indicate the standard deviation over the four simulations for different seeds.

close before the 90% quantile. This artifact is a result of the vascular degeneration where excessively long branches are pruned such that their aspect ratio drops below $\theta_b = 0.9$. In this work, the branch length statistics was chosen heuristically as a showcase. Further analysis of real vasculatures is required to investigate the relationship of branch lengths and vessel diameter in more detail.

Similar to the prescribed branch length statistics, the intrinsic optimality of bifurcation configurations has been validated as measured by angular deviation. Since, by design, bifurcations are constructed with optimal angular configuration, distal bifurcations (small Strahler order) show the smallest deviations. In comparison to bifurcations close to the root (large Strahler order), they are more likely to be created at a rather late stage of the tree construction and hence less exposed to remodeling effects impairing the optimality of the bifurcation configuration. In total, the angular deviations stay below the correction threshold $\theta_a = 5^\circ$.

The semi-log plots of the Strahler order against the average frequency of Strahler vessels, their average length and diameter, respectively, almost follow a linear relationship, which indicates the fractal nature of the synthetic trees. Cassot et al. (2006) have performed a similar analysis on cerebrovascular networks of the human cortex with very similar findings but still better linear fits of the semi-log plots. In our results, the distribution of the Strahler vessel length, in particular, deviates significantly from the linear assumption with large standard deviations over the different trees (see Fig. 9c). This is mainly caused by degenerate trees that are affected by simulation artifacts at the boundaries. Due to the “bottom-up” definition of the Strahler system, the orders have to be computed for the uncropped trees, i.e., including vessel segments outside the ROI. Therefore, the degenerated structures at the boundaries are included in the analysis and spoil the distributions.

Another interesting result is revealed by the analysis of the microvascular structure. The average capillary density as measured by the total microvascular volume fraction and length density is strongly correlated with the metabolic profile (see Fig. 10). This is comprehensible from a physiological point of view, since oxygen delivery takes place at the capillary level for the most part. Larger vessels with thicker vessel walls constrain oxygen diffusion into the tissue. Very similar findings on the correlation of metabolic demand and capillary density have been reported in Weber et al. (2008) for the microvascular system of the macaque visual cortex. The sensitivity of the tree construction is remarkable, considering the fact that the relative metabolic level as defined by the COX-profile ranges from 1 to 1.4 times the base consumption rate as compared to the baseline model at constant level 1.

The angiogenesis-based construction is affected by the microvascular structures since they contribute most to the oxygenation of the surrounding tissue. However, the employed binary tree model is not able to model real network-like capillary structures. Therefore, the results of the microvascular analysis have to be interpreted carefully. A quantitative comparison of our results with the figures of the study by Weber et al. (2008) clearly indicates that the vascular density of our trees is smaller by a factor of two to three. This can partly be explained by the fact that the venous system is not modeled in this work and hence not included in our analysis. Besides, there are different possibilities to adjust the simulation parameters in order to specifically increase the microvascular density, e.g., by reducing the perfusion radius. This would still not resolve the shortcoming of the underlying binary tree model, though. Explicitly modeling network-like microvascular structures would require a more general graph model.

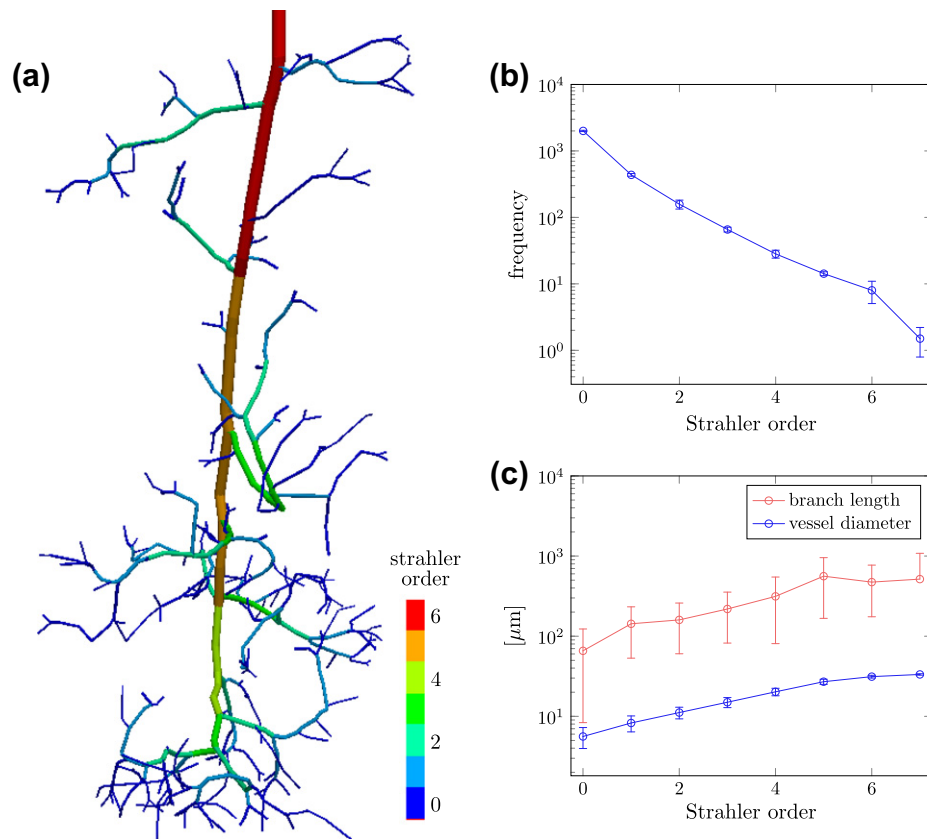


Fig. 9. Branching pattern according to the diameter-defined Strahler order. (a) Visualization of a single connected component. The vessel segments are color-coded according to their Strahler order. (b) Total number of Strahler vessels and Strahler branches in the entire simulation domain. The numbers are averaged over the four simulations with different seeds. (c) Average branch length and diameter of Strahler vessels of successive orders. The numbers are averaged over all Strahler vessels of all four simulations. The error bars indicate the standard deviation (be aware of the log-scale). (For interpretation of the references to color in this figure legend, the reader is referred to the web version of this article.)

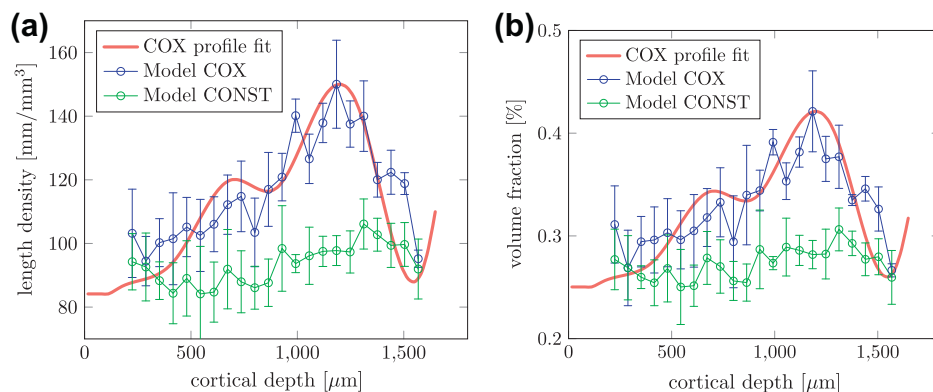


Fig. 10. Comparison of quantitative values of the microvascular system between the COX-based metabolism model (blue) and the reference experiment (green) assuming constant metabolic demand throughout the entire simulation domain. The average length density (a) and volume fraction (b) of the microvascular system is computed across the cortical depth (distance to cortex surface). The error bars indicate the standard deviation over the four simulations per model. The COX profile is overlaid in bold red (dimensionless). (For interpretation of the references to color in this figure legend, the reader is referred to the web version of this article.)

The fluid-dynamic analysis of the constructed trees provides further insight into the functional properties. For the default simulation parameters ($m_b = 14, \gamma = 3.0$) we found that the flow velocities exceed the reference values reported by Lipowsky (2005) by a factor of about 1.5 (see Fig. 11b). As the pressure values at the boundaries, i.e., root and leaf nodes, have been set according to the reference values, the total pressure drop from the feeding vessels to the capillaries remains constant. The flow is hence purely determined by the morphology of the tree structure. Therefore,

the increased blood flow rates clearly indicate that the overall resistance of our trees is too small compared to real vasculatures. The resistance of a single branch is directly proportional to the branch length. An obvious possibility to increase the overall resistance is provided by the choice of the branch length statistics. In fact, the velocity profiles for increased values of the average branch length m_b show smaller flow values especially for large branches.

Another strong assumption of our approach is Murray's law which is intrinsically enforced at each bifurcation node.

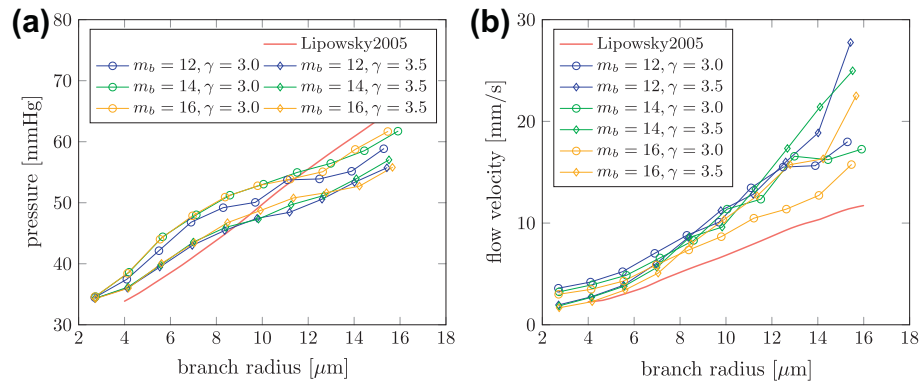


Fig. 11. Fluid-dynamic properties of the tree models with regard to the average pressure (a) and blood flow velocity (b) over branch radius. The profiles are plotted for different values of the average branch length m_b and Murray exponent γ with an overlay of the reference values from Lipowsky, 2005.

Table 2

Comparison of oxygen inflow Q^+ and outflow Q^- for different values of the average branch length m_b , Murray exponent γ , and metabolic models.

m_b	γ	Metabolic model	Q^+ (pl/s)	Q^- (pl/s)	Q^+/Q^-	Q^+ const/cox	Q^- const/cox
12	3.0	const	1609 ± 108	219	7.34	0.824	0.830
		cox	1952 ± 44	264	7.39		
	3.5	const	1113 ± 179	219	5.08		
		cox	1184 ± 65	264	4.48		
14	3.0	const	1099 ± 92	219	5.02	0.850	
		cox	1293 ± 99	264	4.90		
	3.5	const	761 ± 70	219	3.47		
		cox	961 ± 144	264	3.64		
16	3.0	const	873 ± 117	219	3.98	0.867	
		cox	1007 ± 51	264	3.81		
	3.5	const	621 ± 60	219	2.83		
		cox	682 ± 97	264	2.58		

Morphometric analysis of real vasculatures has revealed different values for the Murray exponent ranging from $\gamma = 2.0$ to $\gamma = 3.0$ (Arts et al., 1979; Fung, 1997; Schreiner and Buxbaum, 1993; Zamir, 2000). In another study of the human cerebral cortex, Cassot et al. (2009) found a large spread in the distribution of Murray exponents with an average value of $\gamma = 3.59$. From that, the authors concluded that Murray's law is acceptable as macroscopic approximation but does not appropriately model the architecture of cerebrovascular bifurcations. For the tree generation, increasing the value of the Murray exponent allows to form trees with more bifurcation levels. Comparing the fluid-dynamic properties of the trees for different Murray exponents and constant average branch length shows that the flow at the feeding vessels increases substantially as the total resistance of the tree dropped (see Fig. 11). At the same time, the average flow at the terminal segments decreases, which means that the pressure drop at the microvascular level relative to the large vessels has declined.

The presented angiogenesis model includes different simplifications concerning the reaction–diffusion model for oxygen and VEGF transport. Also, the fluid-dynamic properties of the tree are not incorporated into the construction process. Therefore, the simulated profiles and resulting concentration maps have to be considered as approximations to guide the construction. Accurate computations of the oxygenation require more sophisticated multiphysics simulations which is computationally infeasible at construction time. On a global scale, however, the comparison of the total amount of oxygen delivered by the tree and the expected metabolic demand of the tissue serves as a first plausibility check. In line with the flow velocity profiles, the figures in Table 2 indicate an oxygen excess, i.e., the trees provide more oxygen than demanded by the tissue ($Q^+/Q^- > 1$). The oxygen excess is a direct result of the increased velocity profiles. For increasing segment

length (larger resistance), the total amount of oxygen delivered decreases. For the increased Murray exponent $\gamma = 3.5$, the oxygen excess ratio decreases even further. The relative comparison of oxygen supply and demand for different metabolic models (Q^- const/cox, Q^+ const/cox) shows good agreement of the values, in general. For the standard parameter set, the ratio of the total amount of oxygen delivered by the tree for constant and COX-based metabolism is 0.85 in average. The expected value as given by the ratio of oxygen demand is 0.83. This indicates once more that the oxygen excess is the result of a systematic error, which is mainly attributed to the lack of capillary complexity in our tree model. Nonetheless, it is unreasonable to expect a perfect match of oxygen supply and consumption since the vasculature should be able to handle short-term fluctuations of the metabolic demand without major remodeling.

5. Conclusions

We presented an iterative multi-scale approach for the construction of optimized 3-D arterial tree models based on physiological principles. The driving force of our simulations is a simplified angiogenesis model using case-specific information about the metabolic demand of the tissue in the considered domain. Besides, branch length statistics and morphological optimality principles are incorporated into the construction process.

Synthetic vasculatures were generated in an experimental setup geared to the cerebral anatomy and physiology. Our experiments demonstrated the ability of the construction algorithm to build optimized arterial trees under prescribed morphological and metabolic constraints. We analyzed the structural and functional properties of the tree structures and compared our findings to other studies on the cerebrovascular structure. Clearly,

additional comparison to real data will be needed for full validation of the proposed method. A fluid-dynamic analysis revealed consistent oxygen excess as a systematic error in the oxygen supply which is mainly attributed to the lack of capillary complexity captured by our arterial tree model.

Further improvements can be expected from an advanced vascular tree model which allows for network-like structures at the microvascular scale and anastomoses. However, this transition implies a fundamental redesign of the construction process since the capillary bed inherently has different structural and functional properties as compared to arterioles and arteries. A hybrid modeling approach using an explicit model for precapillary structures and an implicit model for the capillary bed might be an option to reduce the overall complexity.

Another challenge which has not been addressed in this work is the construction of the venous vasculature that matches the arterial side. In principle, the venous counterpart could be constructed based on the same principles with potentially adjusted statistics as it is well known that arteries and veins have slightly different structure. Mutually connecting the terminal segments of the arterial and venous tree would ultimately produce a vascular network. Additional mechanisms such as “inter-vessel” signaling might be required to match the terminal segment density.

We have started to investigate the possibility to adapt the proposed method to be used for the reconstruction of physiologically consistent full-fledged vascular networks from high-resolution image data (Reichold et al., 2009). Within this context, a lot of information on the vessel morphology and topology is extracted from the images. These data open up new opportunities to replace or extend missing or faulty regions by synthetic vasculatures to overcome shortcomings of the reconstruction technique or limitations of the imaging modality.

Acknowledgments

This work has been performed within the frame of the Swiss National Center of Competence in Research on Computer Aided and Image Guided Medical Interventions (NCCR Co-Me) supported by the Swiss National Science Foundation.

Appendix A. Numerical implementation of the angiogenesis model

In this section we will provide more details on the implementation of the simplified angiogenesis model that has been introduced in Section 2.2. Essentially, we will show how to compute the oxygen perfusion map and the corresponding steady-state VEGF

concentration map for a given arterial tree. We will use approximate solutions to the governing reaction–diffusion equations rather than perform full-fledged multiphysics simulations. This is for mainly two reasons. First of all, the reaction–diffusion system has to be computed frequently in our iterative tree construction framework, which renders elaborate multiphysics simulations computationally infeasible. Secondly, the total oxygenation map depends on the fluid dynamics of the vasculature that had to be simulated as well to obtain accurate results. Since we deal with evolving and partly incomplete vascular trees in our construction framework, it remains unclear how to set reasonable boundary conditions for these vasculatures in order to solve the hemodynamics.

The oxygenation map for a given vascular tree is approximated by superposition as follows. Let us first consider a vascular tree consisting of a single vessel segment embedded in tissue with constant metabolic demand. For this simplified vasculature, we solve the reaction–diffusion problem defined in Eq. (4) assuming radial O_2 diffusion with a Dirichlet boundary condition on the surface of the artery wall. The oxygen concentration inside the vessel lumen is in fact considered constant $c_{O_2}^0 = 203.9 \mu\text{l/ml}$, assuming $s_{O_2} = 100\%$, $c_{Hb} = 15 \text{ g/dl}$, and $p_{O_2} = 95 \text{ mmHg}$ using the notation of Eq. (17) (Boas et al., 2008). The O_2 concentration c_1^0 on the surface of the artery wall was chosen heuristically as a function of the vessel radius r :

$$c_1^0(r) = \kappa \frac{r}{r_0} \exp\left(1 - \frac{r}{r_0}\right). \quad (\text{A.1})$$

The function is plotted in Fig. A.12a. The value of c_1^0 can be considered as the “perfusion capability” that is attributed to a given vessel. It peaks for small vessels with capillary radius r_0 : $c_1^0(r_0) = \kappa$ and quickly declines for larger vessels. The peak perfusion level was chosen as $\kappa = 2\%c_{O_2}^0$. This choice corresponds to a maximum O_2 diffusion distance in tissue of approximately $100 \mu\text{m}$ (Secomb et al., 2004; Bauer et al., 2007) for $r_0 = 3.5 \mu\text{m}$ and $R_1^0 = R_{O_2}^{\text{base}}$ (see Fig. A.12b).

The numerical simulations have been implemented in the commercially available simulation software Comsol Multiphysics (Comsol, xxxx). The computed steady-state oxygen concentration maps are illustrated in Fig. A.12b, for different levels of c_1^0 and R_1^0 .

These basic simulations have been computed for constant metabolic demand of the surrounding tissue. In our tree construction framework, however, we have to deal with spatial variations of the oxygen metabolism, in general. Due to the very limited diffusivity of oxygen in tissue, the perfused area of a single vessel segment is likewise very limited as can be seen from Fig. A.12b. If we assume the metabolic activity of tissue to be locally smooth, we

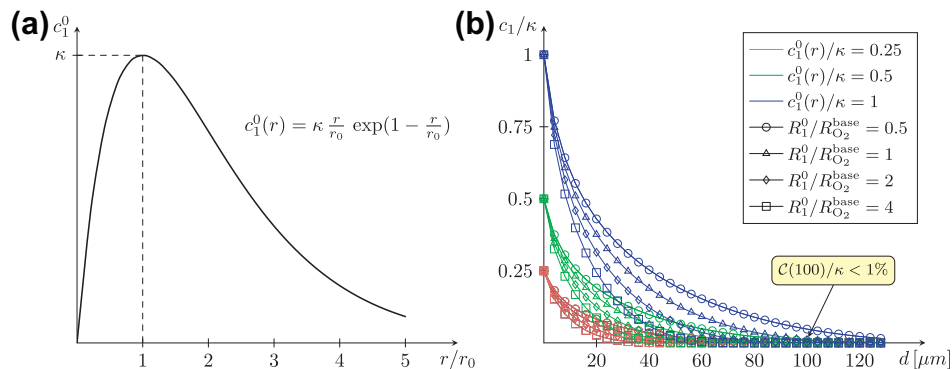


Fig. A.12. (a) Radius-dependent oxygen concentration at the surface of an arterial wall used as Dirichlet boundary conditions for simulations. (b) Steady-state oxygen concentration c_1 for varying metabolic saturation levels R_1^0 and different vessel radii r as a function of the distance d to the vessel surface.

may approximate the steady-state oxygen concentration as a function of the distance to the vessel surface and the local metabolic demand. We implement this approximate computation scheme by precomputing a set of perfusion profiles for different vessel radii and metabolic activities such as those illustrated in Fig. A.12b. These profiles are then assembled to a big look-up table (LUT) which finally allows us to compute the oxygenation by a single vessel segment at any point of the simulation domain for given metabolic map \mathcal{M} using linear interpolation between the closest LUT profiles. For more complex arterial trees consisting of a multitude of vessel segments, we approximate the total oxygenation by superimposing the individual perfusion maps of each single tree segment.

Given the total oxygenation map, we subsequently compute an approximate solution to the VEGF reaction–diffusion problem given in Eq. (9). In this problem, each tissue cell (voxel) acts as a source secreting VEGF at a distinct rate which is defined in Eq. (6) as a function of the local O_2 concentration. For now, let us consider this problem for a single point source, i.e., a single tissue cell emitting VEGF at a fixed rate while surrounded by non-emitting cells. Fig. A.13 shows the steady-state solution to this simplified problem as a function of the distance to the VEGF point source. Moreover, we note that the solution linearly scales with the (constant) VEGF secretion rate. In other words, if the concentration profile \mathcal{C} is solution to the the problem for secretion rate R_2^0 , then $\alpha\mathcal{C}$ solves for αR_2^0 .

Coming back to the original problem with each cell representing a source, we again use superposition as approximate solution to the reaction–diffusion problem. With the definitions of the previous paragraph we thus obtain:

$$c_2(\vec{x}) = \int_{\Omega} \frac{R_2(\vec{s})}{R_2^0} \mathcal{C}(\|\vec{x} - \vec{s}\|) d\vec{s}, \quad (\text{A.2})$$

where Ω denotes the simulation domain. In order to efficiently compute a discrete version of this superposition solution, we essentially approximate the profile function as a weighted sum of Gaussians with an additional correction term:

$$\hat{\mathcal{C}}(\vec{x}) = \omega_0 \delta_{0,x} + \omega_1 \mathcal{G}_1(\vec{x}) + \omega_2 \mathcal{G}_2(\vec{x}), \quad (\text{A.3})$$

ω_i are constant scaling factors, δ denotes the Kronecker delta, and $\mathcal{G}_i = \mathcal{G}(\vec{x}; \sigma_i)$ the Gaussian kernel with standard deviation σ_i and zero mean. The parameters are computed by solving the weighted least-square problem:

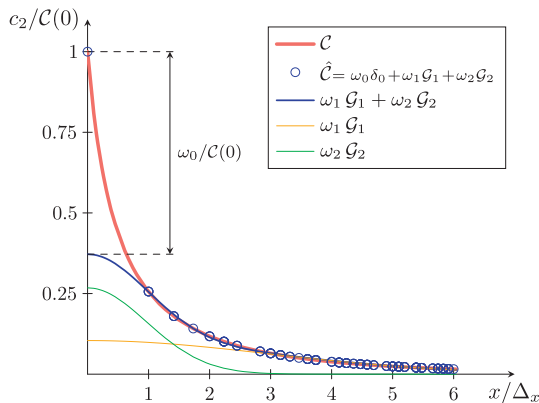


Fig. A.13. Normalized steady-state VEGF concentration profile \mathcal{C} as a function over the Euclidean distance x to the VEGF source (single point source). The radial symmetric profile can be discretized and approximated by a weighted sum of Gaussians $\hat{\mathcal{C}}$ on a discrete 3-D grid with isotropic voxel spacing Δ_x . The function values at the discrete samples are marked by circles.

$$\begin{aligned} \hat{\omega}, \hat{\sigma} &= \operatorname{argmin}_{\omega, \sigma} \int_{\mathbb{R}^3} \frac{1}{\|\vec{x}\|^2} \left(\mathcal{C}(\|\vec{x}\|) - \hat{\mathcal{C}}(\|\vec{x}\|) \right)^2 d\vec{x} \\ &\approx \operatorname{argmin}_{\omega, \sigma} \sum_{\vec{x} \in \Delta_x \mathbb{N}^3} \frac{1}{\|\vec{x}\|^2} \left(\mathcal{C}(\|\vec{x}\|) - \hat{\mathcal{C}}(\|\vec{x}\|) \right)^2, \end{aligned} \quad (\text{A.4})$$

where Δ_x denotes the step size corresponding to the (isotropic) voxel spacing of the discretized simulation domain. The approximated VEGF concentration profile $\hat{\mathcal{C}}$ is illustrated in Fig. A.13. Even though the approximation is inappropriate in the interval $(0, \Delta_x)$, these values will never be used in the implementation.

Plugging the approximated profile of Eq. (A.3) into Eq. (A.2) yields

$$\begin{aligned} c_2(\vec{x}) &= \int_{\Omega} \frac{R_2(\vec{s})}{R_2^0} \hat{\mathcal{C}}(\|\vec{x} - \vec{s}\|) d\vec{s} = \frac{1}{R_2^0} \int_{\Omega} R_2(\vec{s}) \hat{\mathcal{C}}(\|\vec{x} - \vec{s}\|) d\vec{s} \\ &= \frac{1}{R_2^0} (\hat{\mathcal{C}} * R_2)(\vec{x}) \\ &= \frac{1}{R_2^0} \left[\omega_0 R_2(\vec{x}) + (\omega_1 \mathcal{G}_1 + \omega_2 \mathcal{G}_2) * R_2 \right](\vec{x}), \end{aligned} \quad (\text{A.5})$$

where $*$ denotes the convolution operator. In effect, the computation of the discrete VEGF concentration map essentially boils down to simple convolution operations that can be computed efficiently due to the separability of the Gaussian kernels.

As specified in Eq. (9), VEGF is subject to decay with rate v . More precisely, VEGF decrease is due to natural decay on the one hand and uptake by endothelial cells (EC) on the other (Milde et al., 2008). The decay rate employed in Eq. (9) hence can be written as $v = v_0 + v_{\text{EC}} c_{\text{EC}}$, where v_0 denotes the natural decay rate, c_{EC} the EC concentration, and v_{EC} the VEGF uptake rate. In our approximate VEGF diffusion model we assume a homogeneous EC concentration, which renders the computation of the VEGF concentration independent of the vascular tree model, in particular, and set $v = 4v_0$.

This concludes finally the numerical implementation of the simplified angiogenesis model which is summarized in Algorithm 1.

Algorithm 1. Angiogenesis Model → Section 2.2, Appendix A

Require: arterial tree \mathcal{T} , simulation domain Ω , metabolic map \mathcal{M}

- 1: // Perfusion map c_1
- 2: $c_1 \leftarrow 0^{|\Omega|}$ // initialize to zero
- 3: **for all** voxels \vec{x} in Ω **do**
- 4: **for all** tree segments s in \mathcal{T} **do**
- 5: $\vec{p} \leftarrow$ orthogonal projection of \vec{x} onto segment s
- 6: **if** \vec{p} inside s **then**
- 7: $c_s \leftarrow$ LUT($\|\vec{x} - \vec{p}\|$, $\mathcal{M}(\vec{x})$) using linear interpolation
- 8: $c_1(\vec{x}) \leftarrow c_1(\vec{x}) + c_s$
- 9: **end if**
- 10: **end for**
- 11: **end for**
- 12: // VEGF concentration map c_2
- 13: $R_2 \leftarrow$ VEGF secretion map (c_1) Eq. (6)
- 14: $c_2 \leftarrow 1/\alpha \left[\omega_0 R_2 + (\omega_1 \mathcal{G}_1 + \omega_2 \mathcal{G}_2) * R_2 \right]$ Eq. (A.5)
- 15: **return** (c_1, c_2)

Appendix B. Algorithms for the iterative tree construction

In this section, we provide pseudo code for the different algorithms used for iterative tree construction. The algorithm parameters are provided in Table B.3.


```

7:  end for
8:  // Prune leaf nodes with low VEGF signal
9:  //  $O_2$  perfusion map  $c_1$ , VEGF concentration map  $c_2$  ( $c_1, c_2$ )
   ← angiogenesis model ( $\mathcal{T}, \Omega, \mathcal{M}$ )    Appendix A
10: for all leaf nodes  $\bar{p}$  in  $\mathcal{T}$  do
11:   if  $c_2(\bar{p}) < \theta_c$  and  $\theta_v > \mathcal{U}(0, 1)$  then
12:     $s \leftarrow$  leaf segment proximal to  $\bar{p}$ 
13:     $\mathcal{T} \leftarrow$  prune terminal segment ( $s, \mathcal{T}$ )    Algorithm 7
14:   end if
15: end for
16: // Degenerate excessively long leaf branches
17: for all leaf nodes  $\bar{p}$  in  $\mathcal{T}$  do
18:    $p_b \leftarrow$  bifurcation probability at node  $\bar{p}$     Eq. (11)
19:   if  $p_b > \theta_b$  then
20:     $s \leftarrow$  leaf segment proximal to  $\bar{p}$ 
21:     $\mathcal{T} \leftarrow$  prune terminal segment ( $s, \mathcal{T}$ )    Algorithm 7
22:   end if
23: end for
24: return  $\mathcal{T}$ 

```

Algorithm 7. Prune Terminal Vessel

→ Section 2.5

Require: terminal vessel branch/segment s , arterial tree \mathcal{T}

```

1: // Remove node from tree
2:  $\bar{b} \leftarrow$  source node of vessel segment/branch  $s$ 
3:  $\mathcal{T} \leftarrow$  remove vessel branch/segment  $s$  from  $\mathcal{T}$ 
4: // Transition bifurcation node → inter node
5: if  $\bar{b}$  is inter node then
6:   // Avoid sharp bendings
7:    $\bar{p} \leftarrow$  source node of proximal segment of  $\bar{b}$ 
8:    $\bar{q} \leftarrow$  target node of distal segment of  $\bar{b}$ 
9:   relocate inter node  $\bar{b} \leftarrow 0.5 \cdot (\bar{p} + \bar{q})$ 
10:  // Correct distal subtrees
11:   $r_p \leftarrow$  radius of proximal segment of node  $\bar{b}$ 
12:   $r_d \leftarrow$  radius of distal segment of node  $\bar{b}$ 
13:  rescale distal subtree radii of  $\bar{b}$  by  $r_p/r_d$ 
14: end if
15: return  $\mathcal{T}$ 

```

Appendix C. Supplementary material

Supplementary data associated with this article can be found, in the online version, at [doi:10.1016/j.media.2012.04.009](https://doi.org/10.1016/j.media.2012.04.009).

References

- Arts, T., Kruger, R.T., van Gerven, W., Lambregts, J.A., Reneman, R.S., 1979. Propagation velocity and reflection of pressure waves in the canine coronary artery. *Am. J. Physiol.* 237, H469–H474.
- Bauer, A.L., Jackson, T.L., Jiang, Y., 2007. A cell-based model exhibiting branching and anastomosis during tumor-induced angiogenesis. *Biophys. J.* 92, 3105–3121.
- Boas, D.A., Jones, S.R., Devor, A., Huppert, T.J., Dale, A.M., 2008. A vascular anatomical network model of the spatio-temporal response to brain activation. *NeuroImage* 40, 1116–1129.
- Bui, A.V., Manasseh, R., Liffman, K., Sutalo, I.D., 2010. Development of optimized vascular fractal tree models using level set distance function. *Med. Eng. Phys.* 32, 790–794.
- Cassot, F., Lauwers, F., Fouard, C., Prohaska, S., Lauwers-Cances, V., 2006. A novel three-dimensional computer-assisted method for a quantitative study of microvascular networks of the human cerebral cortex. *Microcirculation* 13, 1–18.
- Cassot, F., Lauwers, F., Lorthois, S., Puwanarajah, P., Cances-Lauwers, V., Duvernoy, H., 2010. Branching patterns for arterioles and venules of the human cerebral cortex. *Brain Res.* 1313, 62–78.
- Cassot, F., Lauwers, F., Lorthois, S., Puwanarajah, P., Duvernoy, H., 2009. Scaling laws for branching vessels of human cerebral cortex. *Microcirculation* 16, 1–15.
- Cohn, D., 1954. Optimal systems: I. The vascular system. *Bull. Math. Biol.* 16, 59–74.
- Comsol, A.B., xxxx. Comsol multiphysics. <<http://www.comsol.com/>>.
- Fung, Y.C., 1997. *Biomechanics*, second ed. Springer, New York.
- Gabhan, F.M., Ji, J.W., Popel, A.S., 2007. VEGF gradients, receptor activation, and sprout guidance in resting and exercising skeletal muscle. *J. Appl. Physiol.* 102, 722–734.
- Gafiychuk, V.V., Lubashevsky, I.A., 2001. On the principles of the vascular network branching. *J. Theor. Biol.* 212, 1–9.
- Guibert, R., Fonta, C., Plouraboué, F., 2010. Cerebral blood flow modeling in primate cortex. *J. Cereb. Blood Flow Metab.* 30, 1860–1873.
- Heinzer, S., Krucker, T., Stampanoni, M., Abela, R., Meyer, E.P., Schuler, A., Schneider, P., Müller, R., 2006. Hierarchical microimaging for multiscale analysis of large vascular networks. *NeuroImage* 32, 626–636.
- Heinzer, S., Kuhn, G., Krucker, T., Meyer, E., Ulmann-Schuler, A., Stampanoni, M., Gassmann, M., Marti, H.H., Müller, R., Vogel, J., 2008. Novel three-dimensional analysis tool for vascular trees indicates complete micro-networks, not single capillaries, as the angiogenic endpoint in mice overexpressing human vegf(165) in the brain. *NeuroImage* 39, 1549–1558.
- Ji, J.W., Tsoukias, N.M., Goldman, D., Popel, A.S., 2006. A computational model of oxygen transport in skeletal muscle for sprouting and splitting modes of angiogenesis. *J. Theor. Biol.* 241, 94–108.
- Kaimovitz, B., Huo, Y., Lanir, Y., Kassab, G.S., 2008. Diameter asymmetry of porcine coronary arterial trees: structural and functional implications. *Am. J. Physiol. Heart Circ. Physiol.* 294, H714–H723.
- Kamiya, A., Togawa, T., 1972. Optimal branching structure of the vascular tree. *Bull. Math. Biophys.* 34, 431–438.
- Karch, R., Neumann, F., Neumann, M., Schreiner, W., 1999. A three-dimensional model for arterial tree representation, generated by constrained constructive optimization. *Comput. Biol. Med.* 29, 19–38.
- Karch, R., Neumann, F., Neumann, M., Schreiner, W., 2000. Staged growth of optimized arterial model trees. *Ann. Biomed. Eng.* 28, 495–511.
- Kassab, G.S., 2007. Design of coronary circulation: a minimum energy hypothesis. *Comput. Method Appl. Mech. Eng.* 196, 3033–3042.
- Kassab, G.S., Rider, C.A., Tang, N.J., Fung, Y.C., 1993. Morphometry of pig coronary arterial trees. *Am. J. Physiol.* 265, H350–H365.
- Kaufhold, J., Tsai, P.S., Blinder, P., Kleinfeld, D., 2008. Threshold relaxation is an effective means to connect gaps in 3D images of complex microvascular networks. In: *Proceedings of the 3rd Workshop on Microscopic Image Analysis with Applications in Biology*.
- Klarbring, A., Petersson, J., Torstenfelt, B., Karlsson, M., 2003. Topology optimization of flow networks. *Comput. Method Appl. Mech. Eng.* 192, 3909–3932.
- Kretowski, M., Bézy-Wendling, J., Coupe, P., 2007. Simulation of biphasic ct findings in hepatic cellular carcinoma by a two-level physiological model. *IEEE Trans. Biomed. Eng.* 54, 538–542.
- Kretowski, M., Rolland, Y., Bézy-Wendling, J., Coatrieux, J.L., 2003. Physiologically based modeling of 3-D vascular networks and CT scan angiography. *IEEE Trans. Med. Imag.* 22, 248–257.
- Kurz, H., Burri, P.H., Djonov, V.G., 2003. Angiogenesis and vascular remodeling by intussusception: from form to function. *News Physiol. Sci.* 18, 65–70.
- LaBarbera, M., 1990. Principles of design of fluid transport systems in zoology. *Science* 249, 992–1000.
- Lauwers, F., Cassot, F., Lauwers-Cances, V., Puwanarajah, P., Duvernoy, H., 2008. Morphometry of the human cerebral cortex microcirculation: general characteristics and space-related profiles. *NeuroImage* 39, 936–948.
- Leeuwen, G.M.V., Kotte, A.N., Lagendijk, J.J., 1998. A flexible algorithm for construction of 3-d vessel networks for use in thermal modeling. *IEEE Trans. Biomed. Eng.* 45, 596–604.
- Lipowsky, H.H., 2005. Microvascular rheology and hemodynamics. *Microcirculation* 12, 5–15.
- Lloyd, B.A., Szczepa, D., Rudin, M., Székely, G., 2008. A computational framework for modelling solid tumour growth. *Philos. Trans. A: Math. Phys. Eng. Sci.*
- Lloyd, B.A., Székely, G., 2008. Modeling growth saturation in avascular tumors. In: Stamatakis, G., Dionysiou, D. (Eds.), *Proceedings of the Third International Advanced Research Workshop on In Silico Oncology: Advances and Challenges*, pp. 17–19.
- Lorthois, S., Cassot, F., Lauwers, F., 2011. Simulation study of brain blood flow regulation by intra-cortical arterioles in an anatomically accurate large human vascular network. Part i: methodology and baseline flow. *NeuroImage* 54, 1031–1042.
- Meyer, E.P., Ulmann-Schuler, A., Staufenbiel, M., Krucker, T., 2008. Altered morphology and 3D architecture of brain vasculature in a mouse model for Alzheimer's disease. *Proc. Natl. Acad. Sci. USA* 105, 3587–3592.
- Milde, F., Bergdorf, M., Koumoutsakos, P., 2008. A hybrid model for three-dimensional simulations of sprouting angiogenesis. *Biophys. J.* 95, 3146–3160.
- Murray, C.D., 1926. The physiological principle of minimum work: I. The vascular system and the cost of blood volume. *Proc. Natl. Acad. Sci. USA* 12, 207–214.
- Nekka, F., Kyriacos, S., Kerrigan, C., Cartilier, L., 1996. A model of growing vascular structures. *Bull. Math. Biol.* 58, 409–424.
- Plouraboué, F., Cloetens, P., Fonta, C., Steyer, A., Lauwers, F., Marc-Vergnes, J.P., 2004. X-ray high-resolution vascular network imaging. *J. Microsc.* 215, 139–148.
- Powers, W.J., Grubb, R.L., Darriet, D., Raichle, M.E., 1985. Cerebral blood flow and cerebral metabolic rate of oxygen requirements for cerebral function and viability in humans. *J. Cereb. Blood Flow Metab.* 5, 600–608.

- Pries, A.R., Hpfner, M., le Noble, F., Dewhirst, M.W., Secomb, T.W., 2010. The shunt problem: control of functional shunting in normal and tumour vasculature. *Nat. Rev. Cancer* 10, 587–593.
- Pries, A.R., Secomb, T.W., 2005. Microvascular blood viscosity in vivo and the endothelial surface layer. *Am. J. Physiol. Heart Circ. Physiol.* 289, H2657–H2664.
- Reichold, J., Stampanoni, M., Keller, A.L., Buck, A., Jenny, P., Weber, B., 2009. Vascular graph model to simulate the cerebral blood flow in realistic vascular networks. *J. Cereb. Blood Flow Metab.* 29, 1429–1443.
- Risser, L., Plouraboue, F., Descombes, X., 2008. Gap filling of 3-D microvascular networks by tensor voting. *IEEE Trans. Med. Imag.* 27, 674–687.
- Rosen, R., 1967. *Optimality Principles in Biology*. London.
- Schaffer, C.B., Friedman, B., Nishimura, N., Schroeder, L.F., Tsai, P.S., Ebner, F.F., Lyden, P.D., Kleinfeld, D., 2006. Two-photon imaging of cortical surface microvessels reveals a robust redistribution in blood flow after vascular occlusion. *PLoS Biol.* 4, e22.
- Schneider, M., Hirsch, S., Weber, B., Székely, G., 2011. Physiologically based construction of optimized 3-D arterial tree models. In: Fichtinger, G., Martel, A., Peters, T. (Eds.), *Medical Image Computing and Computer-Assisted Intervention – MICCAI 2011*. Springer, Berlin/Heidelberg, pp. 404–411.
- Schreiner, W., Buxbaum, P.F., 1993. Computer-optimization of vascular trees. *IEEE Trans. Biomed. Eng.* 40, 482–491.
- Secomb, T.W., Hsu, R., Park, E.Y.H., Dewhirst, M.W., 2004. Green's function methods for analysis of oxygen delivery to tissue by microvascular networks. *Ann. Biomed. Eng.* 32, 1519–1529.
- Szczerba, D., Székely, G., 2005. Simulating vascular systems in arbitrary anatomies. In: *MICCAI, 8th International Conference*. Springer, pp. 641–648.
- Tsai, P.S., Kaufhold, J.P., Blinder, P., Friedman, B., Drew, P.J., Karten, H.J., Lyden, P.D., Kleinfeld, D., 2009. Correlations of neuronal and microvascular densities in murine cortex revealed by direct counting and colocalization of nuclei and vessels. *J. Neurosci.* 29, 14553–14570.
- Tuchschnid, S., Bajka, M., Szczerba, D., Lloyd, B.A., SzTkely, G., Harders, M., 2007. Modelling intravasation of liquid distension media in surgical simulators. *Int. Conf. Med. Image Comput. Comput. Assist. Interv.* 10, 717–724.
- Weber, B., Keller, A.L., Reichold, J., Logothetis, N.K., 2008. The microvascular system of the striate and extrastriate visual cortex of the macaque. *Cerebr. Cortex* 18, 2318–2330.
- Zamir, M., 1976. Optimality principles in arterial branching. *J. Theor. Biol.* 62, 227–251.
- Zamir, M., 2000. *The Physics of Pulsatile Flow*, first ed. Springer, New York.
- Zlokovic, B.V., 2011. Neurovascular pathways to neurodegeneration in Alzheimer's disease and other disorders. *Nat. Rev. Neurosci.* 12, 723–738.